THE SYNTHESIS AND CHARACTERIZATION OF THIOGLYCOLIC ACID AND THIOUREA CAPPED FLUORESCENT ZINC SULFIDE NANOPARTICLES

A THESIS SUBMITTED TO
THE GRADUATE SCHOOL OF NATURAL AND APPLIED SCIENCES
OF
MIDDLE EAST TECHNICAL UNIVERSITY

BY

CEMRE MERTOĞLU

IN PARTIAL FULFILLMENT OF THE REQUIREMENTS
FOR
THE DEGREE OF MASTER OF SCIENCE
IN
CHEMISTRY

JUNE 2021

Approval of the thesis:

THE SYNTHESIS AND CHARACTERIZATION OF THIOGLYCOLIC ACID AND THIOUREA CAPPED FLUORESCENT ZINC SULFIDE NANOPARTICLES

submitted by **CEMRE MERTOĞLU** in partial fulfillment of the requirements for the degree of **Master of Science in Chemistry, Middle East Technical University** by,

Prof. Dr. Halil Kalıpçılar
Dean, Graduate School of **Natural and Applied Sciences** _____

Prof. Dr. Özdemir Doğan
Head of the Department, **Chemistry** _____

Prof. Dr. Mürvet Volkan
Supervisor, **Chemistry, METU** _____

Examining Committee Members:

Prof. Dr. Orhan Atakol
Chemistry, Ankara University _____

Prof. Dr. Mürvet Volkan
Chemistry, METU _____

Prof. Dr. Gülsün Gökağaç Arslan
Chemistry, METU _____

Prof. Dr. Gülay Ertaş
Chemistry, METU _____

Assoc. Prof. Dr. Çağdaş Devrim Son
Biological Sciences, METU _____

Date: 29.06.2021

I hereby declare that all information in this document has been obtained and presented in accordance with academic rules and ethical conduct. I also declare that, as required by these rules and conduct, I have fully cited and referenced all material and results that are not original to this work.

Name, Last name: Cemre Mertoğlu

Signature:

ABSTRACT

THE SYNTHESIS AND CHARACTERIZATION OF THIOGLYCOLIC ACID AND THIOUREA CAPPED FLUORESCENT ZINC SULFIDE NANOPARTICLES

Mertoğlu, Cemre
Master of Science, Chemistry
Supervisor: Prof. Dr. Mürvet Volkan

June 2021, 75 pages

The changes in mitochondrial bioenergetics due to DNA mutations lead to an increase in the significance of mitochondria imaging of cancer cells. Since fluorescent imaging provides high resolution, sensitivity, and selectivity to many targets in living cells, fluorescent nanoparticles can be used as imaging probes. Zinc is one of the essential elements in cells used for cell growth, division, and apoptosis. Therefore, zinc sulfide semiconductor nanoparticles have been attracted attention due to its characteristic optical, chemical, and physical properties as well as low toxicity.

In this study, it was aimed to synthesize surface functionalized zinc sulfide semiconductor nanoparticles for mitochondria targeting and imaging of cancer cells. Thioglycolic acid and thiourea capped zinc sulfide nanoparticles were synthesized in an aqueous medium at room temperature. The synthesized zinc sulfide nanoparticles were coated with triphenylphosphonium cation, a targeting moiety, through carbodiimide crosslinking. The fluorescence emission peak of thioglycolic acid and thiourea capped zinc sulfide nanoparticles was at 648 nm. Triphenylphosphonium coated zinc sulfide nanoparticles showed an emission

maximum at 650 nm. The morphological characterization of the surface functionalized zinc sulfide nanoparticles was performed by Transmission Electron Microscopy. Surface functionalization of triphenylphosphonium coated zinc sulfide nanoparticles was performed by heparin and glucose coating, and they were used for intracellular analysis. Intracellular analysis is started to be performed and in progress.

Keywords: Zinc Sulfide Nanoparticles, Triphenylphosphonium, Fluorescence Spectroscopy, Mitochondria Imaging

ÖZ

TİYOGLİKOLİK ASİT VE TİYOÜRE KAPLI FLORESAN ÇİNKO SÜLFİT NANOPARÇACIKLARININ SENTEZİ VE KARAKTERİZASYONU

Mertoğlu, Cemre
Yüksek Lisans, Kimya
Tez Yöneticisi: Prof. Dr. Mürvet Volkan

Haziran 2021, 75 sayfa

Mitokondri görüntüleme, antikanser alanında önem kazanmaktadır çünkü mitokondrideki DNA mutasyonları hücresel biyoenerjetikte değişikliklere yol açmaktadır. Floresan görüntüleme, canlı hücrelerdeki birçok hedefe yüksek çözünürlük, hassasiyet ve seçicilik sağladığından dolayı, floresan nanoparçacıklar, hücrelerin görüntülenmesi için kullanılabilir. Çinko, hücre büyümesi, bölünmesi ve apoptoz için kullanılan, hücrelerde bulunan temel elementlerden biridir. Bu nedenle, çinko sülfit yarı iletken nanoparçacıklar, karakteristik optik, kimyasal ve fiziksel özelliklerinin yanı sıra düşük toksisiteleri nedeniyle de dikkat çekmiştir.

Bu çalışmada, kanser hücrelerinin mitokondri hedeflenmesi ve görüntülenmesi için çinko sülfit yarı iletken nanoparçacıklarının farklı yüzey modifikasyonları ile sentezlenmesi amaçlanmıştır. Tiyoglikolik asit ve tiyosulfat kullanılarak kaplanan çinko sülfit nanoparçacıkları, oda sıcaklığında sulu ortamda sentezlenmiştir. Sentezlenen çinko sülfit nanoparçacıkları, bir hedefleme parçası olarak kullanılan trifenilfosfonyum katyonu ile sırasıyla karbodiimit yöntemi kullanılarak kaplanmıştır. Tiyoglikolik asit ve tiyosulfat ile kaplanan çinko sülfit nanoparçacıklarının fluoresan emisyon dalga boyu yaklaşık 648 nm'dir.

Trifenilfosfonyum kaplı çinko sülfit nanoparçacıkları ise 650 nm'de emisyon yapmaktadır. Yüzey modifikasyonu yapılan nanoparçacıkların karakterizasyonu Geçirimli Elektron Mikroskopisi ile yapılmıştır. Heparin ve glikoz ile yüzey kaplaması yapılan trifenilfosfonyum kaplı çinko sülfit nanoparçacıkları hücre içi analizlerde kullanıldı. Hücre içi analiz çalışmaları başlamış olup, devam etmektedir.

Anahtar Kelimeler: Çinko Sülfit Nanoparçacıklar, Trifenilfosfonyum, Fluoresan Spektroskopisi, Mitokondri Görüntüleme

To My Beloved Family

ACKNOWLEDGMENTS

The author owes her most profound gratitude to her supervisor Prof. Dr. Mürvet Volkan, for her persistent help, unwavering guidance, patience throughout the research. Her experiences and valuable advice about the aspects of both academic and social life are gratefully appreciated. Without her extensive knowledge and insightful suggestions, this thesis has hardly been completed.

The author would like to express her greatest appreciation to Doç. Dr. Çağdaş Devrim Son, for his invaluable contribution and supervision in biological analysis. His guidance in cellular applications has been essential during the study.

The author would like to pay her special regards to Dr. Yeliz Akpınar for her helpful and practical suggestions throughout this study. Her full support is deeply appreciated.

The author would like to thank Prof. Dr. Gülay Ertaş for sharing her experiences about academic life and scientific knowledge.

The author expresses her gratefulness to her lab mates, Begüm Avcı and Eda Akın, and former lab mates Merve Nur Güven Biçer and Pakizan Tasman, for their valuable friendship. Their support and help throughout this study are gratefully acknowledged.

The author would also like to thank Canan Höçük Özkan and Sezin Atıcı Özdemir for their friendship and support.

The author wishes to thank all her sincere friends for their accompaniment throughout her university life.

The author wishes to acknowledge the great love and support of her beloved family, Beyhan Mertoğlu, and Mustafa Mertoğlu. Without their caring upbringing, she would not have been the person she is today.

TABLE OF CONTENTS

LIST OF TABLES

TABLES

LIST OF FIGURES

FIGURES

LIST OF ABBREVIATIONS

ABBREVIATIONS	
DCC	*N*,*N*′-Dicyclohexylcarbodiimide, $C_{13}H_{22}N_2$
EDC	N-(3-dimethylaminopropyl)-N′-ethylcarbodiimide, $C_8H_{17}N_3$
FTIR	Fourier-transform infrared spectrometry
Glu-Hep-TPP-TGA-ZnS NPs	Glucose and heparin coating on TPP coated TGA capped zinc sulfide nanoparticles
Hep-TPP-TGA-ZnS NPs	Heparin coating on TPP coated TGA capped zinc sulfide nanoparticles
MUA-ZnS	MUA capped zinc sulfide nanoparticles
TBAH	Tetrabutylammonium hydroxide, $C_{16}H_{37}NO$
TEM	Transmission electron microscopy
TGA	Thioglycolic acid, $C_2H_4O_2S$
TGA-ZnS NPs	TGA capped zinc sulfide nanoparticles
Thiourea-ZnS NPs	Thiourea capped zinc sulfide nanoparticles
TPP	Triphenylphosphonium, $C_{18}H_{16}P^+$
TPP-TGA-ZnS NPs	TPP coated TGA capped zinc sulfide nanoparticles
TPP-Thiourea-ZnS NPs	TPP coated thiourea capped zinc sulfide nanoparticles
ZnS	Zinc Sulfide

CHAPTER 1

INTRODUCTION

1.1 Nanotechnology

Nanotechnology provides syntheses of materials with substantially new properties, analyses, and characterization of them [1], [2]. Particles at small dimensions, nanoparticles, exhibit unique properties which differ from those in the bulk scale [3]. Nanotechnology, as a rapidly developing field of science, has interdisciplinary research areas in chemistry, medicine, biology, and molecular engineering to produce nanoparticles which can be used for targeting, diagnosing, and treating illnesses such as cancer [3], [4].

1.2 Nanoparticles and Capping Agents

1.2.1 Semiconductor Nanoparticles

Nanomaterials having electrical conductivities remain in between metals and insulators are called semiconductors. Semiconductor nanoparticles have diverse quantum mechanical and optical properties due to their small dimensions and high surface to volume ratio [5], [6], [7]. Also, they are subject to research due to their distinctive electrooptical properties such as long-term photostability, size-tunable light emission, continuous and broad absorption spectra, size-dependent narrow emission spectra, high signal brightness, and high light stability [7], [8]. Their distinct size-dependent properties are due to the quantum confinement effects. When the size of a particle becomes very small compared to an electron, the energy levels become discrete. Therefore, the particle follows the principles of quantum mechanical motion. Due to their size-dependent properties, they are used for labeling

and bioimaging purposes [7]. For imaging applications in living cells and organisms, they are 100 times more stable and 20 times brighter than the organic fluorescent dyes [7], [9]. Also, surface modification of the semiconductor nanoparticles provides an enhancement of their fluorescent quantum yields and hinder their aggregation. Surface functionalization with appropriate functional groups provides their application areas to be more integrated into nanotechnology by making them interact with target molecules better for the detection and imaging of the molecules in biological systems [8].

1.2.2 Zinc Sulfide Semiconductor Nanoparticles

When electromagnetic radiation is exposed to a bulk semiconductor material, the electrons move to the conduction band. Due to the formation of electronic defects in the ZnS crystal structure by the dislocating ions, the electrons will fall back to their valance energy levels by passing through the zinc interstitials and sulfur vacancies which are donor levels. When the excited state electrons which are trapped by donor levels relax, the emission occurs [10]. Among the first discovered II-IV semiconductor, zinc sulfide (ZnS) shows notable properties which makes it to be used as biosensors, catalysts, and fluorophores [11]. It can be prepared in the form of thin films, particles, and rods. They exhibit unique magnetic, thermal, optical, and structural properties due to their small dimensions in the nanometer scale [12]. ZnS nanoparticles have distinctive physicochemical properties such as high surface to volume ratio, quantum tunneling and quantum size effect, thermal stability, and nontoxicity [11], [13]. ZnS can exist in two different crystalline forms, zinc blend and wurtzite due to its polymorphism. As shown in Figure 1.1, zinc blend has a face-centered cubic (fcc) system, while wurtzite has a hexagonal close-packed (hcp) form and zinc and sulfide exhibit tetrahedral coordination in both forms [11]. Zinc blend and wurtzite structures have a wide bandgap of 3.54 eV and 3.91 eV, respectively. Wider bandgap provides higher fluorescence efficiency, lower the toxicity, and increase chemical stability [11], [12], [14]. The size of nanoparticles and wavelength

of emitted light indicate the size of the bandgap of semiconductor material. Therefore, the emission wavelength can be controlled by changing the size of the nanoparticles [14], [15].

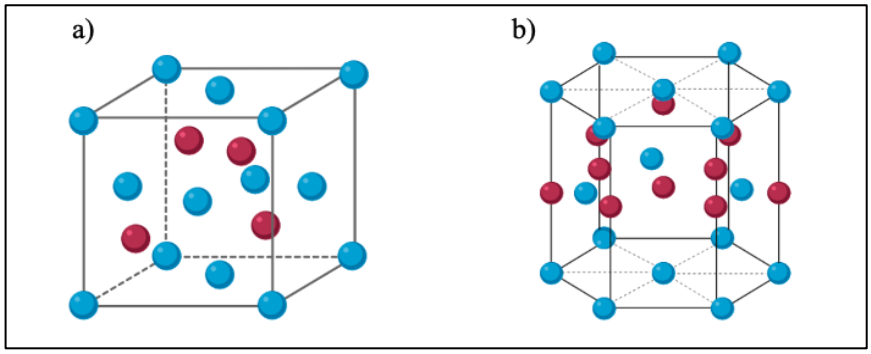

Figure 1.1. ZnS nanoparticles in the form of zinc blend (a) and wurtzite (b) structures

1.2.2.1 The Preparation Methods for ZnS NPs

Nanoparticles can be synthesized by several methods. Top-down and bottom-up methods are the two methods used for the fabrication of nanomaterials. In the top-down method, nanomaterials are obtained from a bulk semiconductor. In the bottom-up method, nanomaterials are obtained from solid, liquid, or gas precursors by chemical reaction [12]. Bhargava et al. [16] reported the synthesis of luminescent nanomaterials by chemical precipitation. They produced manganese doped ZnS nanoparticles by reacting diethyl zinc with hydrogen sulfide, and they obtained 18% quantum efficiency. Ethyl manganese, the dopant, was added to the zinc solution. Methacrylic acid was used as a surfactant to provide sufficient separation between the nanoparticles. The photoluminescence spectra of manganese doped ZnS nanoparticles were obtained at 590 nm. Khosravi et al. [17] prepared manganese doped ZnS nanoparticles in an aqueous medium, using manganese chloride as a dopant. Zinc chloride was mixed with mercaptoethanol and then, manganese

chloride and sodium sulfide added dropwise. Nitrogen gas was used to prevent the oxidation of the nanoparticles. The emission peak was observed at 600 nm. This group also reported the synthesis of ZnS quantum dots in alkaline medium by using copper as a dopant in sodium hexametaphosphate. The phosphate chains prevent the agglomeration of nanoparticles [18]. Karar et al. [19] also synthesized manganese doped ZnS nanoparticles capped with zinc oxide. They mixed zinc acetates with manganese, then with sodium sulfide. The size of manganese doped ZnS nanoparticles were about 4 nm. Their photoluminescence peak was between 550-700 nm. A new method developed by Wang and Hong [20] is called the heat-assisted chemical reaction method for the synthesis of ZnS nanoparticles. They powdered zinc acetate and thioacetamide separately, then mixed them and powdered again to achieve even-sized particles. The reaction was carried out at different temperatures in the range of 80-300 °C. The size of the nanoparticles was approximately 3 nm at 100 °C. The emission wavelength of nanoparticles was around 420 nm. Yang et al. [21] developed a procedure to prepare ZnS nanoparticles doped with cupper and rare earth metals by chemical precipitation from the homogenous solution method. Zinc acetate and the chloride salts of dopants were used as precursors in thioacetamide solution. The temperature of each solution was raised to 80 °C. They were reacted for 30 minutes at pH 2.0. The emission peaks were between 540-550 nm. Another method developed by Stanic et al. [22] was based on synthesizing ZnS nanoparticles by using the sol-gel method. Zinc tert-butoxide and hydrogen sulfide were used as precursors. They dried the gel in a vacuum and characterize it by X-ray diffraction (XRD) and Infrared Spectroscopy. Haranath et al. [23] also synthesized ZnS nanomaterials in porous silica by using stable inorganic capping agents. The silica gel was formed by tetraethylorthosilicate, water, and hydrochloric acid. Silica is mixed with aqueous solutions of zinc and manganese, and sodium sulfide was used for the gel formation. Also, they reported for the first time that the structure of ZnS nanoparticles changed to wurtzite at 900 °C and obtained a broad photoluminescence peak at around 585 nm. Xu et al. [24] reported a method to prepare ZnS nanoparticles, which were responsive to impurities with the hydrothermal method in

the microemulsion. Poly(oxyethylene)$_5$nonyl phenol ether and poly(oxyethylene)nonylphenol ether was used as a surfactant, and the oil phase was petroleum ether. Zinc chloride and sodium sulfide were prepared separately and then mixed with constant stirring. ZnS nanocrystals were synthesized by using copper, europium, and manganese as dopants, and their sizes were around 3 – 18 nm. The luminescence intensity of manganese doped ZnS nanoparticles was higher than the ZnS nanoparticles, which were synthesized in the aqueous medium. The ultrasonic-assisted method was first reported by Xu and Ji [25] to synthesize ZnS nanoparticles. Sodium sulfide was reacted with particles in aqueous solution under ultrasonic radiation. The size of the particles was reported as 40 nm by transmission electron microscopy (TEM) imaging. Potra et al. [26] synthesized wurtzite ZnS nanoparticles at 413 K by using different precursors by microwave-assisted solvothermal method. The nanoparticles were characterized by XRD, TEM, ultraviolet-visible (UV-vis) and photoluminescence (PL) measurements. Also, the possible mechanism of formation was reported. The PL spectra of nanoparticles were at 400 – 800 nm. Xu et al. [27] synthesized manganese doped ZnS nanocrystalline thin films by sputtering method at 1050 °C. The reaction took place for 3 hours in a vacuum tube. The deposition rate was 2 nm per second. Manganese doped ZnS nanoparticles were identified by TEM imaging, and they had a highly oriented structure. The mean size of the nanoparticles was 20 nm.

1.2.2.2 Zinc Sulfide Nanoparticles and Their Biomedical Applications

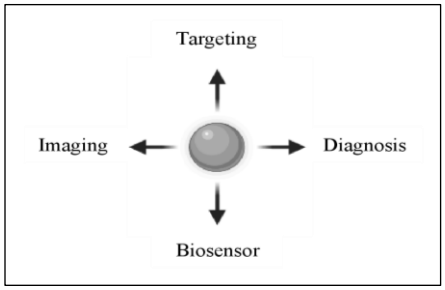

Figure 1.2. Use of nanoparticles for biomedical applications

Nanoparticles can be used in several areas in biomedicine as shown in Figure 1.2. The application of nanomaterials in biomedicine is compelling due to the nanosized components of living cells [28]. Metal nanoparticles such as silver, gold, iron, and zinc are suitable for targeting and diagnostic purposes in biomedicine since their size and structure determine their chemical and physical properties [29]. Also, fine powders of these nanomaterials exhibit biological activity [28]. They not only prevent the aggregation and enhance the stability of particles, but they also target the desired location for diagnostic purposes [28], [30]. The interaction of nanoparticles with living cells is different from the bulk material since their physical and chemical properties become different from their metal compounds. To illustrate, some metal nanoparticles are less toxic on the organism than their metal salts, and less toxicity makes them suitable for biomedical applications [28], [31].

Zinc is one of the most basic elements in cells such that it is essential for cell growth, division, and apoptosis. Hence, its deficiency can affect vital processes in cells. There are two forms in living organisms: reactive zinc ion and bound zinc. It can be used in the form of metallic nanoparticles, zinc, metal and non-metal oxides, zinc oxide, zinc sulfide semiconductor nanoparticles, and quantum dots. ZnS nanoparticles can be used as an alternative to fluorescent organic dyes since they exhibit photostability, biocompatibility, and low toxicity. Also, their fluorescence intensities are high, and they have resistivity to photobleaching. Moreover, real-time observations of molecules in living cells are more probable with nanoparticles than organic dyes. For example, ZnS nanoparticles can be used for identifying the antigens in tumors. When coated with L-cysteine, the sensitive and straightforward detection of proteins in blood serum by synchronous fluorescence is possible. Fluorescence intensity of particles increases with the number of protein molecules present. Detection of biomarkers by using semiconductor fluorescent nanomaterials might be used in nanobiotechnology in the future [28].

1.2.3 Capping Agents

1.2.3.1 N-Terminated Capping Agents

The N-terminated capping agents such as pyridine, quinoline, oleyamine, octadecylamine, and hexadecylamine have nitrogen (N) as a donor atom. For II-VI semiconductor nanoparticles like zinc sulfide, primary amines with long chains are reported as a more suitable surfactant. Not only the ZnS nanoparticles but also hexadecylamine capped cadmium selenide and hexadecylamine capped calcium nanoparticles exhibit high luminescence quantum efficiency and monodispersing properties [32], [33]. Also, octadecylamine provides a size-controlled synthesis of noble metal and metal oxide nanoparticles which are synthesized as a liquid at room temperature by using oleyamine with high stability [32].

1.2.3.2 O-Terminated Capping Agents

Capping agents like oleic acid contain oxygen (O) as a donor atom, which provides coordination with the surface of nanoparticles. In some cases, the oxygen atom in carboxylate can coordinate through a double bond so that the nanoparticles become soluble in polar solvents [32]. For instance, Li et al. [34] showed that capping silver nanoparticles with oleic acid increases their dispersion stability in water.

1.2.3.3 P-Terminated Capping Agents

Tri-n-octylphosphene oxide, triphenylphosphine (TPP), and tri-n-octylphosphine are some of the P-terminated capping agents. Phosphine oxide in tri-n-octylphosphene oxide forms coordination with the cadmium selenide quantum dot surface through the interaction of lone pair of electrons. The hot injection technique is the most common method for the coating of nanoparticles with these capping agents. It

provides an advantage, like enhancing the dispersity of nanoparticles, but the process requires toxic and expensive precursors [32].

1.2.3.4 S-Terminated Capping Agents

Molecules containing sulfur (S) such as thiols are called S-terminated capping agents. Thiols have polar head groups which make nanoparticles to be more biocompatible. Thioglycolic acid (TGA), 2-mercapto ethanol, mercaptopropionic acid and mercapto ethyl amine are examples of thiols. In Figure 1.3, some examples of s-terminated capping agents are shown. The emission intensity of nanoparticles depends on the proper choice of capping agent [32].

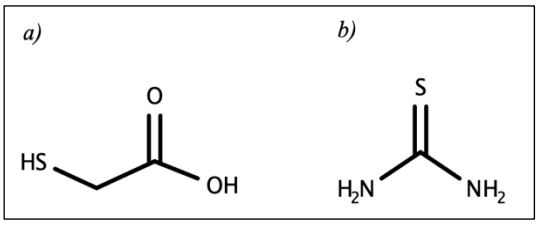

Figure 1.3. Examples of s-terminated capping agents, thioglycolic acid (a) and thiourea (b)

1.2.3.5 Green Capping Agents

Green capping agents such as enzymes, biodegradable polymers, citric acid, vitamins, and polyphenols are essential for providing a green and clean production, reducing the environmental pollution, and making the nanoparticles applicable in many areas like biomedicine, biology, and physical sciences [32], [35]. Polysaccharides such as cellulose, heparin, glucose, and starch are also used as green capping agents. They are composed of several monosaccharide units connected with glycosidic linkages. They sterically stabilize nanoparticles by ion-dipole interactions

between hydroxyl groups and metal ions. The synthesis of nanoparticles is performed in water instead of toxic solvents; thus, it is a green process. [32].

1.2.3.6 Polymers

Poly(ethylene glycol), poly(vinyl pyrrolidine) and poly(vinyl alcohol) are commonly used polymers for the stabilization of nanoparticles by steric and electrostatic effects [32], [36]. Polymers which contain π-electrons form a delocalization system by overlapping of their p-orbitals. Conjugating polymers such as polyacetylene, polyparavinylene, polythiophene, and polyparaphenylene can also be used as a capping agent in bioimaging due to their low toxicity and biocompatibility. Another type of polymeric capping agent is block copolymers, which form nanosized particles containing micelles. Copolymers interact with the carboxylic acid groups of metal ions through their hydrophilic side [32]. Dendrimers are classified as another type of capping agent with unusual symmetry with cavities on the structure, and the nanoparticles are encapsulated by them [32], [37]. This encapsulation enhances the stability of nanoparticles. Poly(amidoamine), and poly(propylene amine)are the most commonly used polymers of this type. Poly(amidoamine) is also used for the synthesis of noble metal nanoparticles as a stabilizer [32].

1.2.4 The Effect of Capping Agents on Nanoparticles

Capping agents are essential for the functionalization and stabilization of nanoparticles. They are used for controlling the size, morphology, and selectivity of nanoparticles for a specific target. Therefore, the surface modification of nanoparticles by capping agents affects their optical properties, morphology, particle size, mechanical stability, toxicity, and photostability [9], [38]. Also, the coating degree, amount, composition, bulkiness, charge, the interaction of capping agents with nanoparticle surface, and with other compounds affect the size, shape,

morphology, and stability of metal nanoparticles. As a result, it is crucial to choose a proper capping agent for the synthesis of metal nanoparticles [39], [40].

Capping agents also provide the synthesis of monodispersed nanoparticles by forming a layer on their surfaces to prevent the aggregation. Metal nanoparticles need to be stabilized due to their tendency to form agglomerates and coagulate in solution by coating them with capping agents such as polymers, small ligands, organic compounds, and polysaccharides. Coating the surface of metal nanoparticles introduce various properties by enhancing their solubility in different solvents and compatibility with different compounds. Also, surface coating with capping agents provides high dispersion, reducing the interaction of nanoparticles with each other in the solution [40]. Therefore, the agglomeration of nanoparticles in solution can be prevented by using capping agents by keeping them colloidal and it makes them suitable candidates for various biological applications [39].

Many capping agents have been reported to synthesize nanoparticles, such as polymers, organic compounds, and surfactants [39], [40]. Several results have been reported about the toxicity levels of nanoparticles in vivo and in vitro studies, and it was concluded that toxicity levels of nanoparticles mostly depend on their sizes. nanoparticles with a size of 10 nm led to more cell death than the ones with a size of 50-100 nm. According to the studies, the toxicity levels of nanoparticles can be reduced by using capping agents [39-43]. Therefore, the selection of proper capping agents is a critical step since the toxicity of capping agents can restrict the application areas of nanoparticles. Different capping agents such as thioglycolic acid, thiourea, mercapto silane, and L-cysteine are used to functionalize nanoparticles. Also, zinc containing nanoparticles are not toxic when they are not very concentrated; they are environmentally friendly and have high surface area compared to their bulk. These properties make ZnS nanoparticles suitable for biomedical applications [9].

1.3 An Introduction to Cancer

1.3.1 Cancer Cell Metabolism

Despite the causes and biological basis of cancer have been studied by scientists, there is not a precise understanding of its metabolism. Therefore, the difference between healthy and cancer cells must be detected to fully understand it [44]. Mitochondrion plays a vital role in cell metabolism and is the primary energy source of the cell. One of the essential functions of it is to produce energy as adenosine triphosphate (ATP) through oxidative phosphorylation (OXPHOS) [45]. Also, it plays an essential role in programmed cell death, cell survival, and the generation of reactive oxygen species (ROS). The disfunction of one of these key aspects leads to mitochondrial diseases such as cancer.

The key essence of cancer is a change in cellular bioenergetics. Otto Warburg explained this phenomenon by 'aerobic glycolysis' known as 'Warburg effect' which is used for the detection and diagnosis of tumors [46]. Healthy cells produce ATP in the mitochondria by OXPHOS. Glucose transporters take glucose through the cell surface, and it is metabolized by glycolysis with the production of pyruvate. Then pyruvate is converted to acetyl-CoA and oxidized to carbon dioxide by tricarboxylic (TCA) cycle in the mitochondrial matrix as shown in Figure 1.4 [47], [48]. The nicotinamide adenine dinucleotide (NADH) and flavin adenine dinucleotide (FADH2) carriers, high-energy electrons, are produced and pass through the electron transport chain as releasing energy, which leads to the formation of the electrochemical proton gradient in the inner mitochondrial membrane. The gradient has potential energy, which leads to the production of ATP. So, ATP is produced by a gradient-driven process, and this is called OXPHOS, which is the production of ATP from glucose in healthy cells [47]. Despite the presence of sufficient oxygen and low energetic yield of glycolysis, ATP is produced by glycolysis in most cancer cells due to its rapid production compared to OXPHOS. Cells synthesize biological molecules to reproduce, and the complete oxidation of

glucose to carbon dioxide and water by the TCA process prevents the usage of glucose for the synthesis of new biological molecules. Cancer cells use glucose for the production of amino acids, lipids, and nucleotides to proliferate instead of complete oxidation of it [47], [48-51]. Glycolysis decreases the sensitivity of cancer cells to permeabilization of the outer mitochondrial membrane, which is essential for apoptosis. As a result, cancer cells become resistant to apoptosis by glycolysis [47].

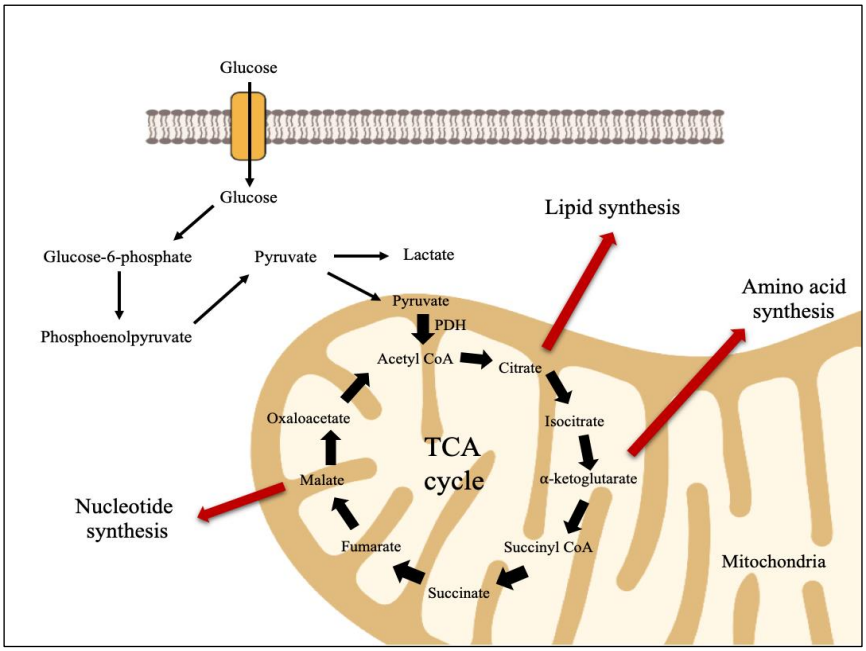

Figure 1.4. Glucose transporters take glucose into the cell, and it is converted to pyruvate by glycolysis. TCA cycle begins with acetyl CoA. The by-products of pyruvate are used in lipid, amino acid, and nucleotide synthesis in cancer cells.

1.3.2 Diagnosis of Cancer

Mitochondria imaging gain importance in the anticancer field, which is in a state of exploration, since deoxyribose nucleic acid mutations in mitochondria lead to changes in the cellular bioenergetics which accompany cancer [46], [52]. In light of this information, novel techniques in cancer detection have been developed. One of

them includes using nanoparticles as biomarkers for targeting the mitochondria and provide sensitive detection of cancer cells [53].

1.3.3 Mitochondria and Mitochondria Targeting Probes

1.3.3.1 The Structure of Mitochondrial Membrane

Mitochondria are composed of inner and outer membranes formed by a phospholipid bilayer. Inner membrane space (IMS) and mitochondrial matrix, the aqueous species inside mitochondria, are separated from each other by these membranes [54]. Their permeabilities to various sized molecules are different from each other. The inner membrane is not permeable to ions and protons, and all substances in the mitochondrial matrix and metabolites pass through IM in an arranged manner. As a result, it forms a proton gradient, which is essential for OXPHOS. Therefore, the presence of a proton gradient is crucial for cellular activities. Moreover, the permeability of the outer membrane (OM) is also well arranged, and it is permeable to small molecules up to 5 kDa [55].

1.3.3.2 The Passage of Molecules Through Mitochondrial Membrane

Scientists are inclined to mitochondria targeting moieties for enhancing the efficiency of the targeting [53]. The higher transmembrane potentials of mitochondria of the cancer cells compared to the ones of the healthy cells provide a negatively charged interior plasma membrane, making the mitochondria targeting compounds to be concentrated in the mitochondria of cancer cells [53], [54], [55]. Cationic compounds firstly penetrate the cytosol and then mitochondria since both the membranes and the plasma of mitochondria have negative membrane potential [51].

Triphenylphosphonium (TPP) cation, a cationic lipid, is suitable for penetrating the mitochondrial membrane due to the delocalized positive charge on its surface [51],

[53], [56]. As a result of the highly negative membrane potential inside, it can penetrate by the interaction of negatively charged plasma membrane with positively charged ions as shown in Figure 1.5. In other words, membrane potential, $\Delta\Psi$, provides the passage of charged compounds through the membrane [51], [57].

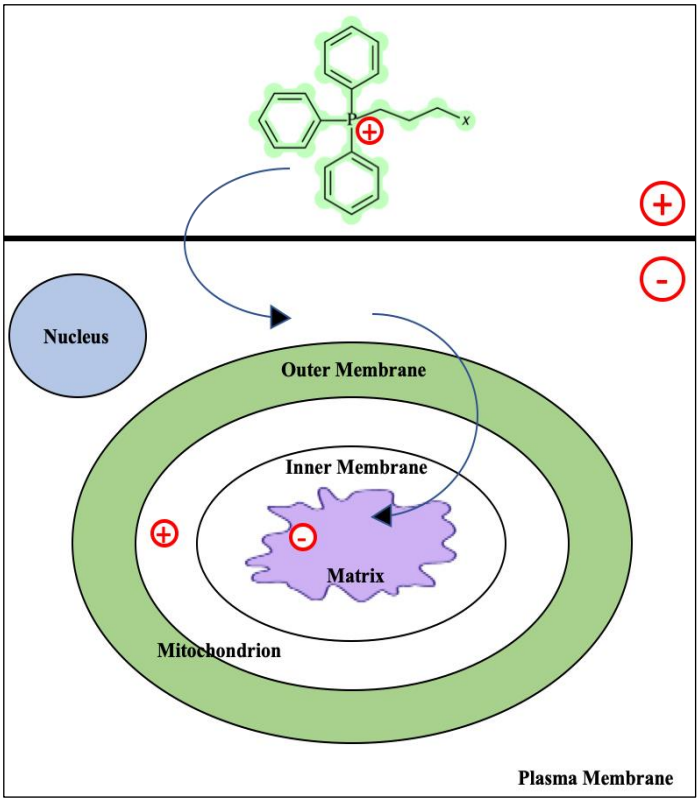

Figure 1.5. The passage of lithophilic cation (TPP) penetrate firstly into cytosol and then the mitochondrion.

Due to the electrostatic interaction between negatively charged phosphate groups and the positively charged mitochondria targeting moiety, lipophilic cations bind to the IMS surface. Their position on the surface depends on hydrophobic and hydrophilic properties of the linkers. As shown in Figure 1.6, lipophilic cations will position themselves on the center of the membrane due to hydrophobic linkers and they move toward the aqueous part of the membrane with hydrophilic linkers. They are transferred to the matrix by phospholipid membrane [54], [58], [59].

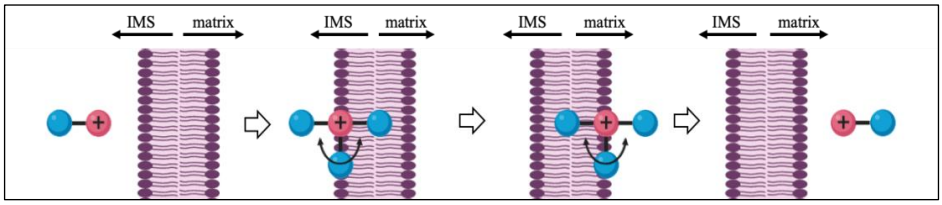

Figure 1.6. The positioning of lipophilic cations on IMS surface by the charge interactions and their passage into the mitochondrial matrix by hydrophobic and hydrophilic linkers.

1.3.3.3 Triphenylphosphonium Cation

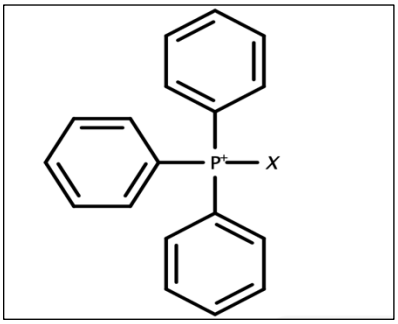

Figure 1.7. The molecular structure of TPP cation.

TPP has three hydrophobic phenyl groups around the positively charged phosphorus atom as shown in Figure 1.7. TPP cation has several advantages as a mitochondrion targeting moiety for the delivery of small compounds into mitochondria. TPP is stable in most biological systems due to its low reactivity toward cell components. It does not require a protein transporter to move into the mitochondria due to its hydrophobic surface, and a delocalized positively charge on a large surface. Also, it is easy to synthesize and purify it, and its light absorption and emission in visible or near-infrared region are relatively low. Due to these advantages, TPP cation is used for several applications, such as imaging the mitochondria of cells [54].

1.3.4 Detection and Imaging

Cancer cells are clinically detected by analyzing their morphological properties. There are several clinical imaging techniques, such as magnetic resonance imaging, X-ray, tomography, endoscopy, and mammography. These methods are not sensitive enough to separate the normal and cancerous tissue. Also, they are unable to detect cancer in its early stages, making early detection of the disease a main challenge [60]. Nanotechnology provides the synthesis of nanoparticles exhibiting distinctive properties, which can reduce the detection time of cancer. Therefore, using these nanomaterials in the clinic can provide rapid detection of the disease [60], [61]. Fluorescent nanoparticles can be used for the imaging of the cells since fluorescence imaging provides high temporal and special resolution, sensitivity, and selectivity to many targets in living cells [60], [62], [63].

1.4 Aim of the Study

Our purpose was to synthesize functionalized fluorescent nanoparticles with different capping agents for the targeting and imaging of cancer cells. For this purpose, ZnS semiconductor fluorescent nanoparticles, which have distinct surface modifications, were synthesized. ZnS nanoparticles have been capped with TGA and thiourea to obtain acid and amine capped surfaces. Then, TGA and thiourea capped ZnS nanoparticles are coated with mitochondria targeting moiety, TPP, by using(3-hydroxypropyl) triphenylphosphonium (TPP-$(CH_2)_3$-OH) and (5-carboxypentyl) triphenylphosphonium (TPP-$(CH_2)_5$-COOH) for the penetration of surface functionalized fluorescent ZnS nanoparticles into the mitochondria. TPP-$(CH_2)_3$-OH was attached to the surface of TGA capped ZnS nanoparticles by esterification reaction. Likewise, TPP-$(CH_2)_5$-COOH was attached to the surface of thiourea capped ZnS nanoparticles through carbodiimide coupling. After the glucose and heparin coating on the surface of TPP coated TGA capped ZnS nanoparticles, N2a cell lines were used for in vitro analysis. The intracellular analysis is in progress.

CHAPTER 2

EXPERIMENTAL

2.1 Instrumental

2.1.1 Centrifuge

NÜVE NF 200 Small Centrifuge was used for precipitating TGA capped, thiourea capped and TPP coated ZnS nanoparticles. TGA and thiourea capped ZnS nanoparticles were centrifuged at 5000 rpm for 20 minutes. TPP coated ZnS nanoparticles were centrifuged for 45 minutes at 5000 rpm.

2.1.2 Ultrasonic Cleaning Unit

Elma Elmasonic S 40 Ultrasonic Bath was used to prevent the agglomeration of TGA capped, thiourea capped and TPP coated ZnS nanoparticles.

2.1.3 Ultrasonic Liquid Processor

Vibra-Cell ultrasonic liquid processor probe was used to prevent the agglomeration of TGA capped, thiourea capped and TPP coated ZnS nanoparticles.

2.1.4 Vortex Mixer

HEIDOLPH Reax Top VORTEX was used to prepare homogenously dissolved solutions.

2.1.5 Fluorescence Spectrometry

Hitachi F-2500 Fluorescence Spectrophotometry was used for determining the relative emission intensities and wavelengths of TGA capped, thiourea capped and TPP coated ZnS nanoparticles when excited at 323 nm.

2.1.6 Fourier-Transform Infrared Spectrometry

The functional groups on the surface of the TGA capped, thiourea capped and TPP coated ZnS nanoparticles were characterized by Alpha, Bruker Fourier Transform Spectroscopy. Pellets prepared from KBr was used for the sample preparation. The 4 cm^{-1} resolution was used. 10 measurements were taken for each sample.

2.1.7 Zeta Potential and Zeta Sizer Measurements

The hydrodynamic size and surface potential of the TGA capped, thiourea capped and TPP coated ZnS nanoparticles were determined by Malvern Nano ZS90.

2.1.8 Transmission Electron Microscopy

Jem Jeol 2100F 200kV HRTEM located at METU Central Laboratory was used for the characterization of surface modified ZnS nanoparticles.

2.1.9 Scanning Electron Microscopy

QUANTA 400F Field Emission SEM located at METU Central Laboratory was used for the characterization of the functionalized ZnS nanoparticles.

2.1.10 X-ray Diffractometer (XRD)

XRD measurements of the TGA-ZnS NPs were performed by using a Rigaku Mini-Flex X-ray powder diffractometer with a Cu Ka line radiation (λ = 1.54056 Å) source. For characterization, samples were air dried.

2.1.11 ImageJ Software

The average diameter of one hundred randomly selected nanoparticles were determined by using ImageJ software. Then, the size distribution graphs were drawn according to the data obtained.

2.2 Chemicals and Reagents

For the whole experimental procedure, 18.2 MΩ.cm ultrapure (Type 1) deionized water provided by ELGA LabWater, Purelab Option-Q water purification system was used.

2.2.1 Preparation of TGA Capped ZnS (TGA-ZnS) NPs

Thioglycolic acid ($HSCH_2COOH$, 98%, SIGMA-ALDRICH), Sodium sulfide hydrate ($Na_2S.xH_2O$, technical, ≥60% RT, flakes, SIGMA-ALDRICH), Zinc nitrate hexahydrate ($H_{12}N_2O_{12}Zn$, crystalline/certified, FISHER SCIENTIFIC), Tetrabutylammonium hydroxide ($C_{16}H_{37}NO$, EGA CHEMIE) were used.

2.2.2 Preparation of Thiourea Capped ZnS (Thiourea-ZnS) NPs

Zinc nitrate hexahydrate ($H_{12}N_2O_{12}Zn$, crystalline/certified, FISHER SCIENTIFIC), Sodium sulfide hydrate ($Na_2S.xH_2O$, technical, ≥60% RT, flakes, SIGMA-

ALDRICH), Thiourea (CH_4N_2S, 99%, crystal, ALLIED CHEMICALS), Nitrogen (N_2, ≥ 99%, gas, LINDE) were used.

2.2.3 Preparation of 11-Mercaptoundecanoic acid (MUA) Capped ZnS (MUA-ZnS) NPs

11-Mercaptoundecanoic acid ($C_{11}O_2H_{23}S$, 95%, SIGMA-ALDRICH), Zinc nitrate hexahydrate ($H_{12}N_2O_{12}Zn$, crystalline/certified, FISHER SCIENTIFIC), Sodium sulfide hydrate ($Na_2S.xH_2O$, technical, ≥60% RT, flakes, SIGMA-ALDRICH), Sodium hydroxide (NaOH, puriss, 97%, pellets, SIGMA-ALDRICH) were used.

2.2.4 Synthesis of TPP Coated TGA Capped ZnS (TPP-TGA-ZnS) NPs by Using (3-hydroxypropyl)triphenylphosphonium

N,N-Dimethylformamide ($HCON(CH_3)_2$,anhydrous, 99.8%, SIGMA-ALDRICH), N,N′-Dicyclohexylcarbodiimide ($C_6H_{11}NCNC_6H_{11}$, SIGMA-ALDRICH), 4-(Dimethylamino)pyridine ($C_7H_{10}N_2$, SIGMA-ALDRICH) were used.

2.2.5 Synthesis of TPP Coated Thiourea Capped ZnS (TPP-Thiourea-ZnS) NPs by Using (5-carboxypentyl)triphenylphosphonium

Sodium hydroxide (NaOH, puriss, 97%, pellets, SIGMA-ALDRICH), N-(3-dimethylaminopropyl)-N′-ethylcarbodiimide hydrochloride (EDC.HCl, for sequence analysis, Fluka), ethanol (CH_3CH_2OH, absolute, ≥99.8%, SIGMA-ALDRICH) were used.

2.2.6 Heparin and Glucose Coating of TPP-TGA-ZnS NPs

Enoxaparin (CLAXENE®), D-Glucosamine hydrochloride ($C_6H_{13}NO_5$.HCl, ≥98%, ACROS Organics) were used.

2.2.7 Cell Growth

N2a Cell Line ATCC (American Type Culture Collection), PBS (pH 7), and N2a cell growth medium were used.

2.3 Procedures

2.3.1 Synthesis of TGA-ZnS NPs

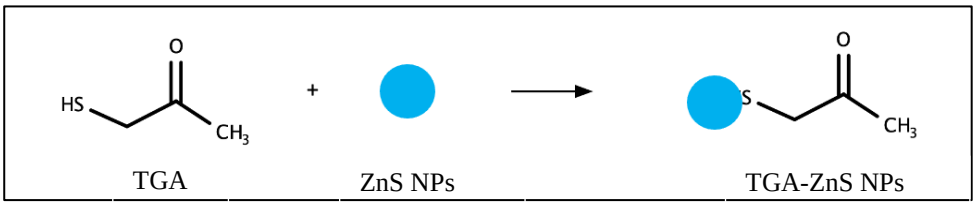

Figure 2.1. The proposed reaction mechanism of TGA-ZnS NPs (ZnS NPs=blue sphere)

TGA capped ZnS nanoparticles (TGA-ZnS NPs) were synthesized by using a simple and green chemistry method as shown in Figure 2.1. 10.0 mL of 0.64 mmol TGA solution was prepared in deionized water. It was continuously stirred at 700 rpm for 5 min. 2.0 mL of 0.8 mmol zinc nitrate hexahydrate ($Zn(NO_3)_2.6H_2O$) solution was added dropwise with constant stirring. Then the mixture was titrated with 1.0 M tetrabutylammonium hydroxide (TBAH) to pH 12. After the solution was stirred for 10 min, 4.0 mL of 0.4 mmol sodium sulfide (Na_2S) was added rapidly into the solution. The solution was stirred for 5 min. The remaining 6.0 mL of $Zn(NO_3)_2.6H_2O$ solution was added dropwise with constant stirring. The pH of the solution was adjusted to 12.0 with 1.0 M TBAH. Then the solution was let to be stirred for 2 hours at room temperature in dark [64]. After the reaction time was ended, the solution became cloudy, indicating the formation of TGA-ZnS NPs as

shown in Figure 2.2. The nanoparticle solution was washed five times with deionized water by centrifugation at 5000 rpm for 20 min in order to get rid of the excess precursors. It was dispersed in water and kept in room temperature for further use. Also, the fluorescence image of TGA-ZnS NPs in comparison with the deionized water under UV light is shown in Figure 2.3.

For the characterization of the TGA-ZnS NPs, potassium bromide (KBr) pellet was prepared for FTIR analysis.

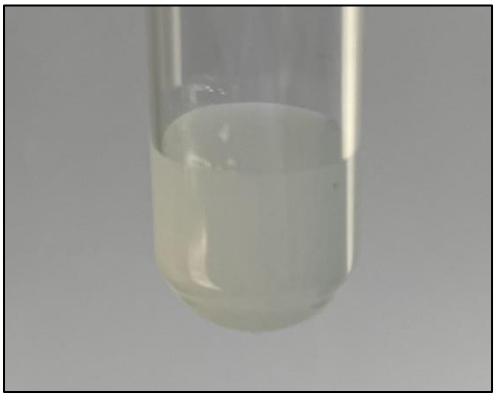

Figure 2.2. The formation of TGA-ZnS NPs

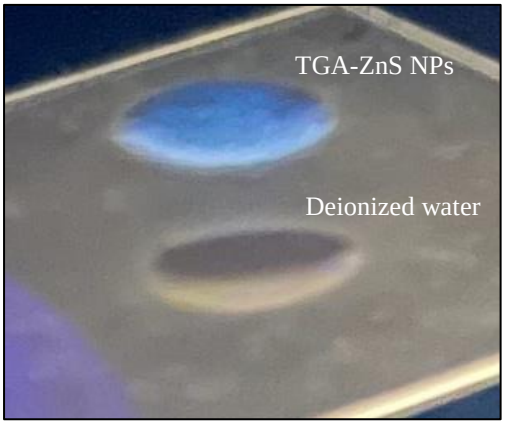

Figure 2.3. The fluorescence image of TGA-ZnS NPs compared to deionized water under UV light (254 nm)

2.3.2 Synthesis of Thiourea-ZnS NPs

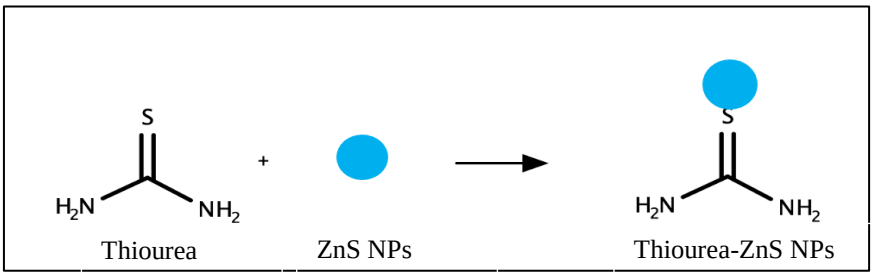

Figure 2.4. The proposed reaction mechanism of Thiourea-ZnS NPs (ZnS NPs=blue sphere)

Figure 2.4 shows the proposed reaction mechanism of Thiourea-ZnS NPs. 5.0 mL of 0.5 mmol $Zn(NO_3)_2.6H_2O$ solution was prepared with deionized water. It was constantly stirred at 700 rpm for 5 min and purged with nitrogen (N_2) gas. 5.0 mL of 0.5 mmol thiourea (NH_2CSNH_2) was added dropwise and the solution was left to be stirred for 10 min under N_2 purging. After 5.0 mL of 0.25 mmol Na_2S was added dropwise, the reaction was carried out for 2 hours at room temperature in dark under N_2 purging [64]. The formation of the thiourea capped ZnS nanoparticles (Thiourea-ZnS NPs) were observed by the cloudy state of the solution as shown in Figure 2.5. After the reaction time was over, the nanoparticle solution was precipitated and washed five times with deionized water by centrifugation at 5000 rpm for 20 min in order to get rid of the excess precursors. It was dispersed in water and kept in room temperature for further use.

For the characterization of the Thiourea-ZnS NPs, KBr pellet was prepared for FTIR analysis.

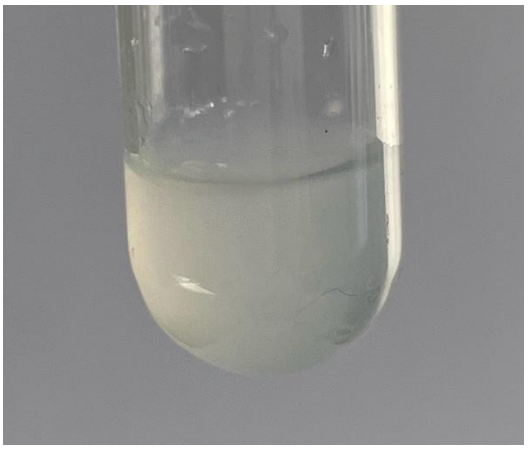

Figure 2.5. The formation of Thiourea-ZnS NPs

2.3.3 Preparation of MUA-ZnS NPs

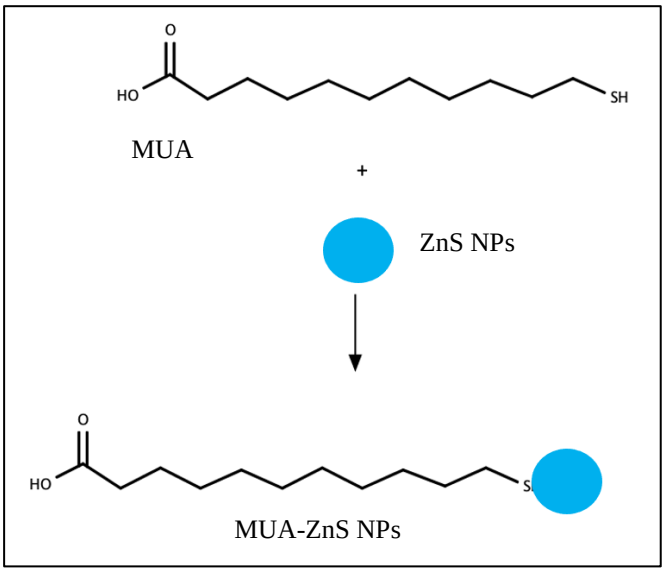

Figure 2.6. The proposed reaction mechanism of MUA-ZnS NPs (ZnS NPs=blue sphere)

The proposed reaction mechanism of MUA-ZnS NPs is shown in Figure 2.6. 0.4 mg/mL of $Zn(NO_3)_2.6H_2O$ solution and 0.5 mg/mL of MUA were dissolved in 60.0 mL of deionized water. The pH of the mixture was adjusted to 12 by NaOH solution. The solution was mixed for 1 h to obtain a cloudy dispersion. After degassed with N_2 gas, 0.5 mg/mL of Na_2S were added to the reaction flask. Then the solution was let to be stirred for 2 hours at room temperature in dark. The nanoparticle solution was washed five times with deionized water by centrifugation at 5000 rpm for 5 min to get rid of the excess precursors.

2.3.4 Synthesis of TPP-TGA-ZnS NPs with (3-hydroxypropyl)triphenylphosphonium

The TPP coated TGA capped ZnS nanoparticles (TPP-TGA-ZnS NPs) were synthesized by esterification reaction between the -OH group of TPP and the -COOH group on the surface of ZnS nanoparticles. For the activation of the -COOH group on the surface of ZnS nanoparticles, *N*,*N*′-Dicyclohexylcarbodiimide (DCC) was used. 1.0 mL of 0.08 mmol TGA-ZnS NPs was stirred at 600 rpm for 5 min. Then, 0.1 mmol of DCC was prepared in 2.5 mL DMF and was added dropwise. The solution of TGA-ZnS NPs and DCC were mixed at constant stirring for 4 hours in room temperature. Then, 0.01 mmol of DMAP and 0.2 mmol of (3-hydroxypropyl)triphenylphosphonium (TPP-$(CH_2)_3$-OH) was prepared in 2.5 mL DMF and was added dropwise. The reaction was carried out for 24 hours at room temperature in dark [65]. The proposed mechanism of the reaction is given in Figure 2.7. The final solution was washed with acetone and ethanol by centrifugation at 5000 rpm for 15 min.

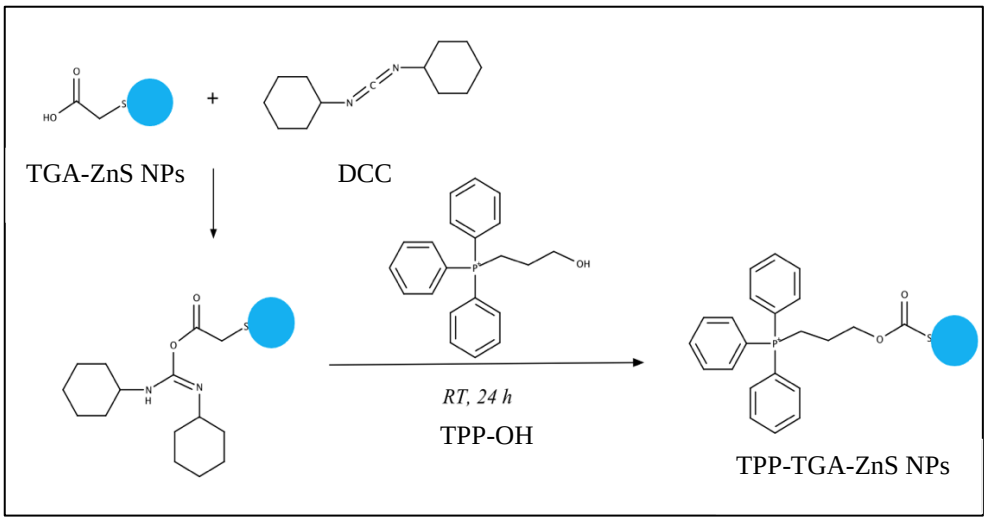

Figure 2.7. The proposed reaction mechanism of the TGA-ZnS NPs (blue sphere) with TPP via DCC reaction

2.3.5 Synthesis of TPP-Thiourea-ZnS NPs with (5-carboxypentyl)triphenylphosphonium

The TPP coated thiourea capped ZnS nanoparticles (TPP-Thiourea-ZnS NPs) were synthesized by N-(3-dimethylaminopropyl)-N′-ethylcarbodiimide hydrochloride (EDC)coupling between the -COOH group of TPP and -NH_2 group of ZnS NPs in alkaline medium. 5.0 mL of 0.5 mmol (5-carboxypentyl)triphenylphosphonium (TPP-$(CH_2)_5$-COOH) solution was prepared with 50% EtOH. It was constantly stirred at 600 rpm for 5 min. The pH of the solution was adjusted to 11.0 with NaOH. Then, 2.0 mL of 0.25 mmol Thiourea- ZnS NPs solution were added dropwise. The solution was mixed for 5 min. 5.0 mL of 0.5 mmol EDC was also prepared in 50% EtOH and added dropwise into the solution. The reaction was carried out for 24 hours at room temperature in dark [66]. The mechanism of the activation process and the proposed mechanism of the reaction is given in Figure 2.8. The final solution was washed five times with 50% EtOH by centrifugation at 5000 rpm for 45 min.

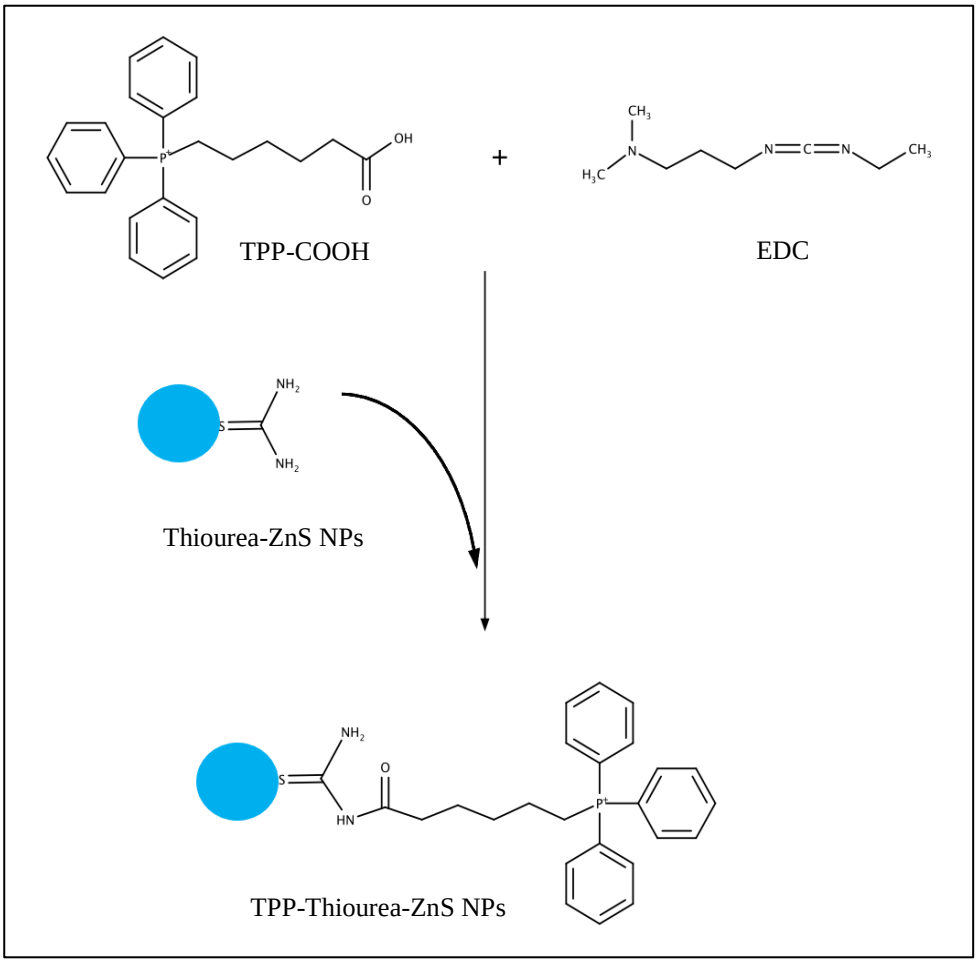

Figure 2.8. The proposed reaction mechanism of the Thiourea-ZnS (blue sphere) with TPP via EDC reaction

2.3.6 Heparin Coating on TPP-TGA-ZnS NPs

2.0 mL of TPP-TGA-ZnS NPs were added to the 0.24 mg/mL of Heparin solution. The reaction was carried out for 12 h. The resulting solution was centrifuged, and Heparin coated TPP-TGA-ZnS NPs (Hep-TPP-TGA-ZnS NPs) were collected.

2.3.7 Glucose and Heparin Coating on TPP-TGA-ZnS NPs

0.5 mM, 2.0 mL EDC and 2.5 mM, 2.0 mL NHS were added to 30.0 mL Heparin solution after one another. After the solution was stirred for 30 mins, 0.5 mg/mL of D-Glucosamine hydrochloride were added to the solution. The reaction was carried out for 2 h. Then, 2.0 mL of TPP-TGA-ZnS NPs were added to the 15.0 mL of Heparin-Glucose solution while sonicating. Then the reaction was carried out for 12 h in dark. The resulting solution was centrifuged, and Glucose-Heparin coated TPP-TGA-ZnS NPs (Glu-Hep-TPP-TGA-ZnS NPs) were collected. The proposed reaction mechanism is given in Figure 2.9.

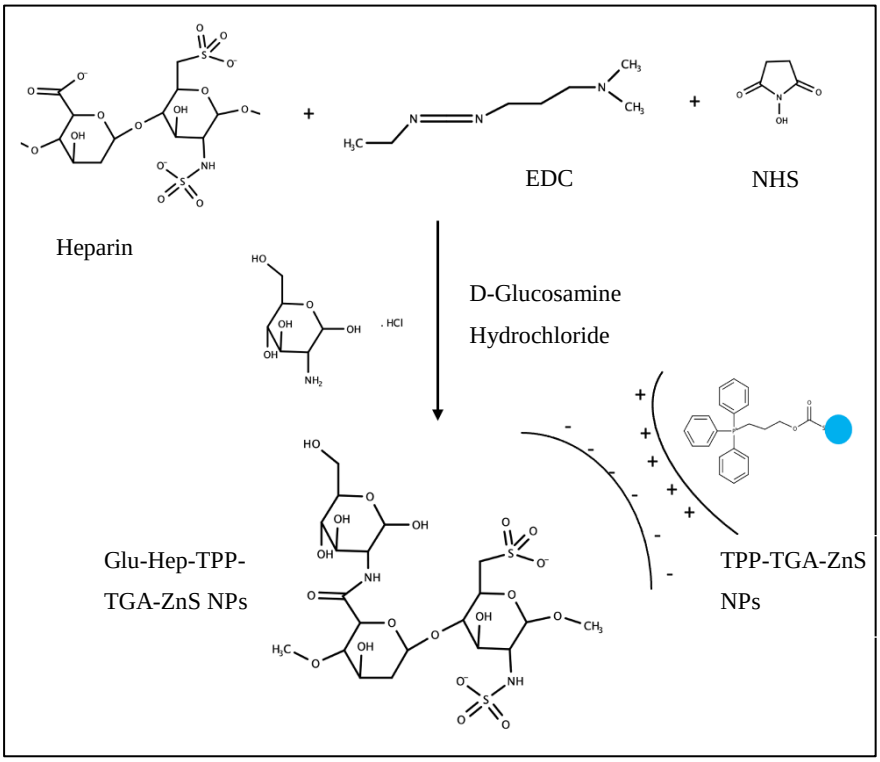

Figure 2.9. The proposed reaction mechanism of the Glu-Hep-TPP-TGA-ZnS (blue sphere) via EDC&NHS reaction

2.4 Biological Experiments

Biological experiments were carried out in the Department of Biological Sciences at METU under the supervision of Assoc. Prof. Dr. Çağdaş Devrim Son.

CHAPTER 3

RESULTS AND DISCUSSION

In the scope of this thesis, surface-functionalized semiconductor ZnS nanoparticles were synthesized with various shape and size in an aqueous medium at room temperature. Their fluorescence properties were analyzed by Fluorescence Spectroscopy. FTIR spectroscopy and TEM were used for the characterization of the nanoparticles.

3.1 Analysis of TGA-ZnS NPs

Capsule shaped ZnS nanoparticles were synthesized by using TGA as a capping agent for the functionalization, stabilization, and dispersion of the nanoparticles. According to Aliofkhazraei et al. [38], the presence of positive or negative charge on the surface of the small-sized nanoparticles prevents the possible agglomeration. Therefore, the distribution of the nanoparticles in a solution depends on the concentration of the capping agent present on their surface. Due to the negatively charged carboxyl groups on the surface of TGA-ZnS NPs, they repel each other and do not form aggregates [40]. Figure 3.1 shows the transmission electron microscope (TEM) images of TGA-ZnS NPs. The capsule shape and dispersion of the nanoparticles can be seen from the TEM images.

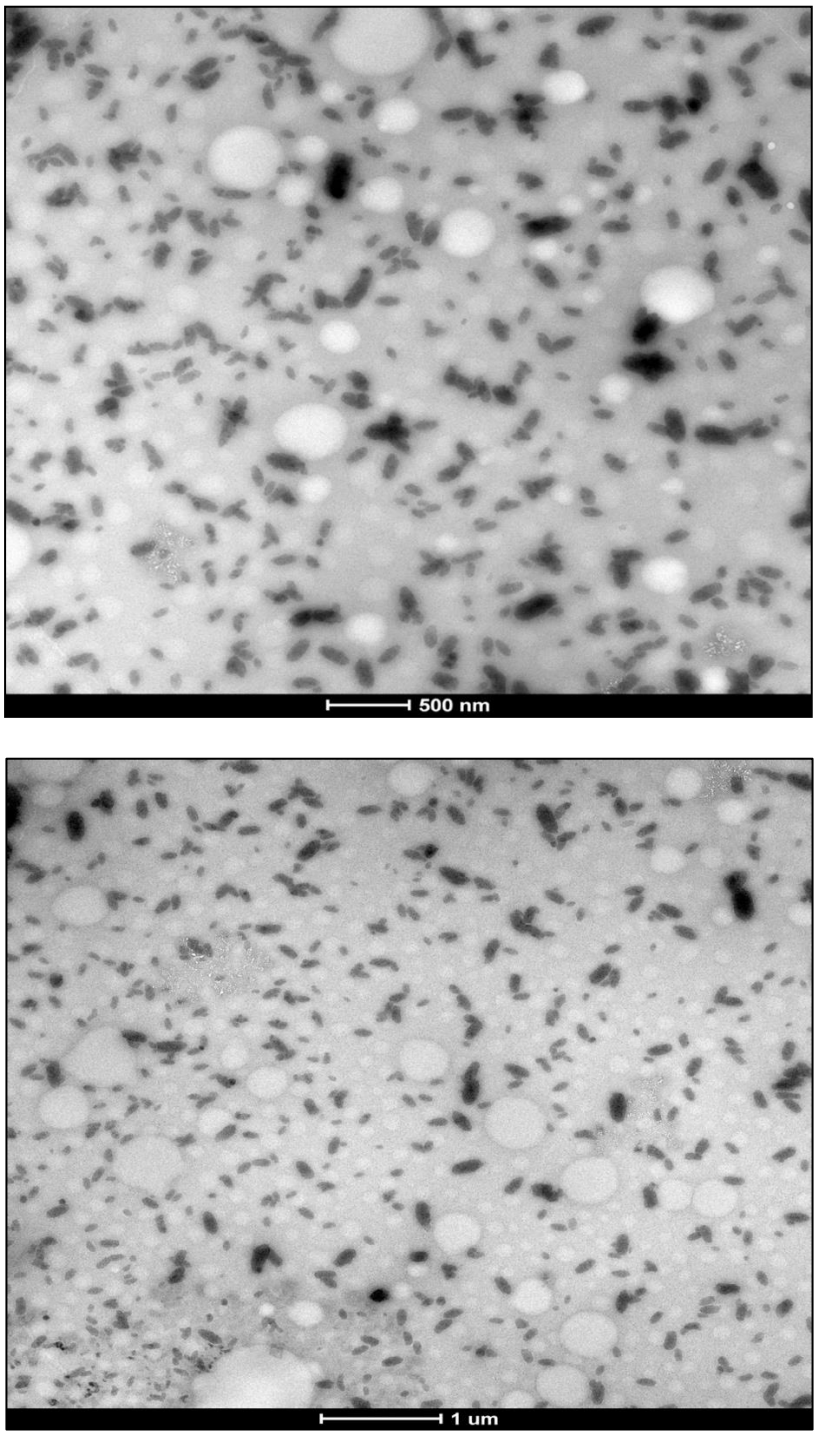

Figure 3.1. TEM images of TGA-ZnS NPs prepared in basic medium

The size distribution of the TGA-ZnS NPs were analyzed by ImageJ software. Except for some large particles, the sizes of the particles are below 105 nm. Two of these large particles are displayed in Figure 3.2. Due to the capsule shape of the TGA-ZnS NPs, the size was calculated in terms of height and width. One hundred five particles were selected from the TEM image to draw the size distribution graphs. The height distribution graph of TGA-ZnS NPs is given in Figure 3.3. According to the figure, the height of the nanoparticles varies between 85-105 nm and the average height is calculated as 92 ± 6 nm. However, the plateau region of the weighted size distribution plot in Figure 3.3 corresponds to 95-100 nm.

The width distribution graph of TGA-ZnS NPs is given in Figure 3.4. According to the figure, the width of nanoparticles varies between 50-60 nm, and the plateau region of the weighted size distribution graph corresponds to the size distribution of 55-60 nm. The mathematical mean width of the particles was calculated as 52 ± 5 nm.

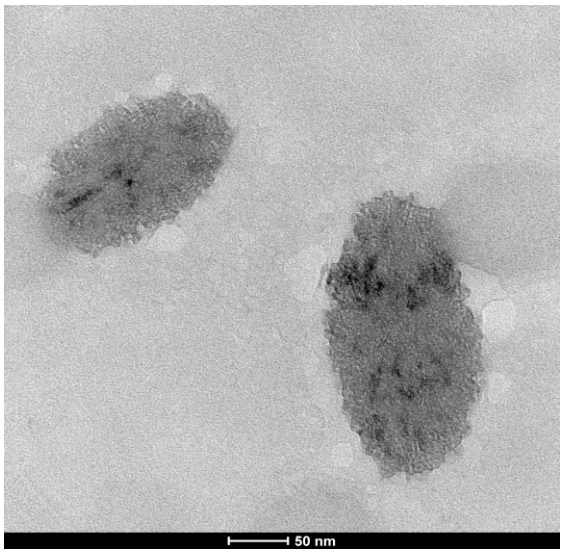

Figure 3.2. The capsule shaped TGA-ZnS NPs

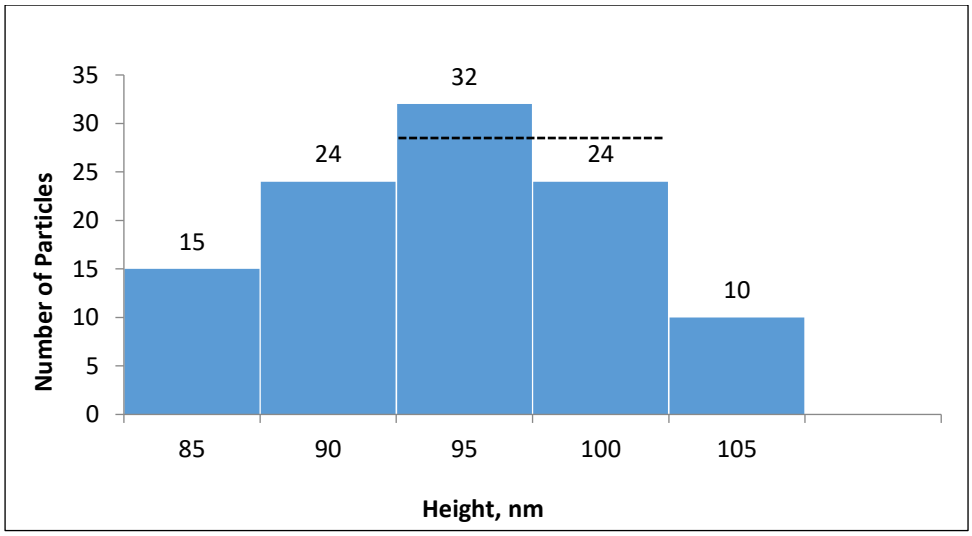

Figure 3.3. Height distribution graph of TGA-ZnS NPs

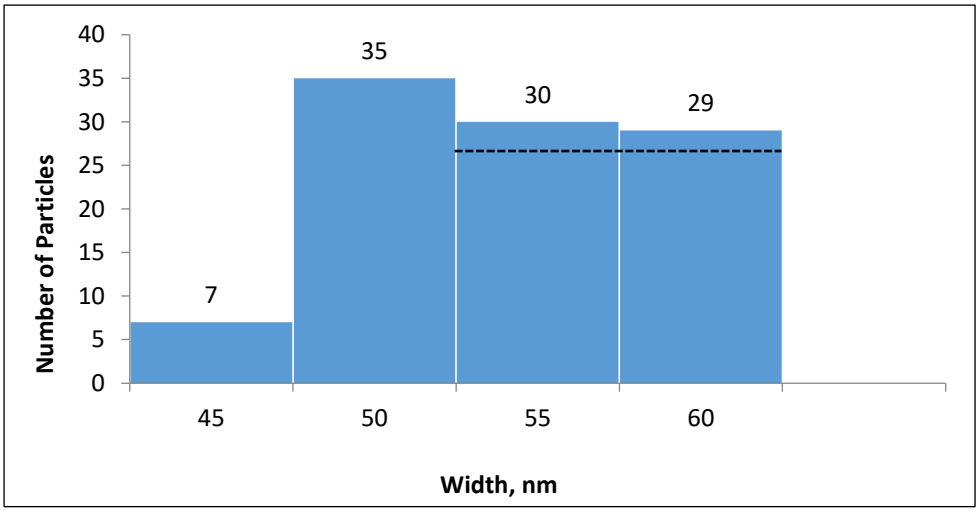

Figure 3.4. Width distribution graph of TGA-ZnS NPs

For the surface characterization of TGA-ZnS NPs, the FTIR spectra of the TGA-ZnS NPs and TGA is given in Figure 3.5. The peaks shown with red arrow are related with the TGA vibrations and the peaks shown with blue arrow are related with the ZnS vibrations. Due to the changes in size and morphology of TGA-ZnS NPs, there are shifts in the FTIR spectrum. The characteristic O-H and C=O stretching

vibrations of carboxylic acids appear at 3244 and 1568 cm^{-1}. The peak at 1228 cm^{-1} indicates C-O stretching of COOH. Finally, the peaks at 711 and 775 cm^{-1} are responsible for the characteristic ZnS stretching. Also, the disappearance of S-H stretching peak at 2568 cm^{-1} shows that TGA binding to the ZnS surface was mediated by sulfur group. These results show that the surfaces of ZnS nanoparticles were coated with TGA groups [64], [65], [71].

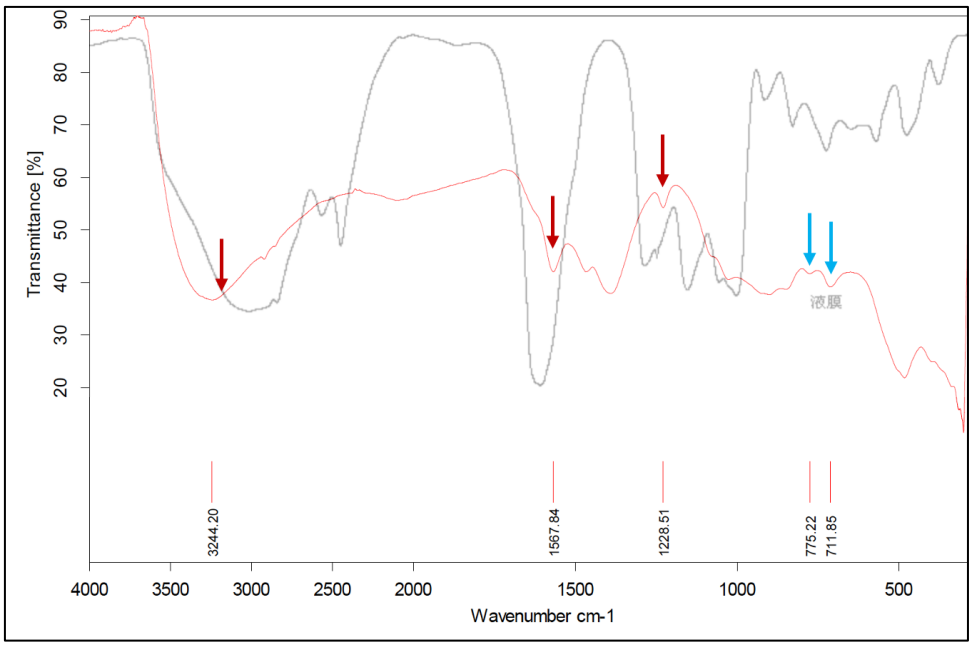

Figure 3.5. FTIR spectrum of TGA-ZnS NPs (red) and TGA (black)

The fluorometric properties of nanoparticles play an essential role in obtaining high resolution, sensitivity, and selectivity for the mitochondria imaging of cancer cells [60], [62], [63]. Also, the success of the nanoparticle synthesis can be determined by the fluorescence measurements. Due to their high fluorescence intensity, especially semiconductor nanoparticles draw attention for biological applications [38]. As shown in Figure 3.6, the nanoparticles exhibit a fluorescence emission maximum at 648 nm when excited at 323 nm with an emission intensity around 1270 relative

fluorescent units (RFU). 5 nm excitation and emission bandwidth were used. The fluorescence spectrum of TGA-ZnS NPs were taken in aqueous solution.

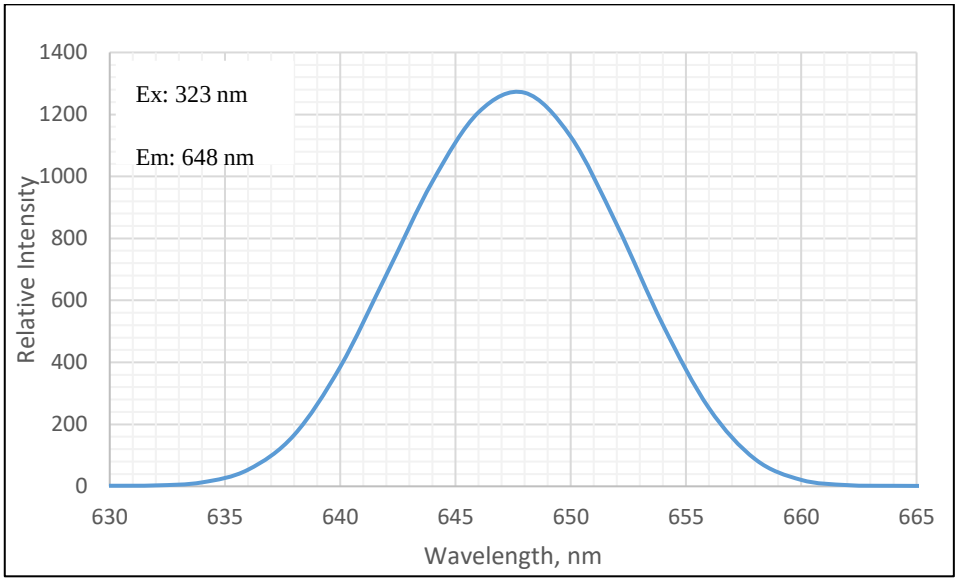

Figure 3.6. Fluorescence spectrum of TGA-ZnS NPs in neutral medium, pH~7

The excitation wavelength of TGA-ZnS NPs was also acquired. As shown in Figure 3.7, the TGA-ZnS NPs exhibit an excitation maximum at 326 nm.

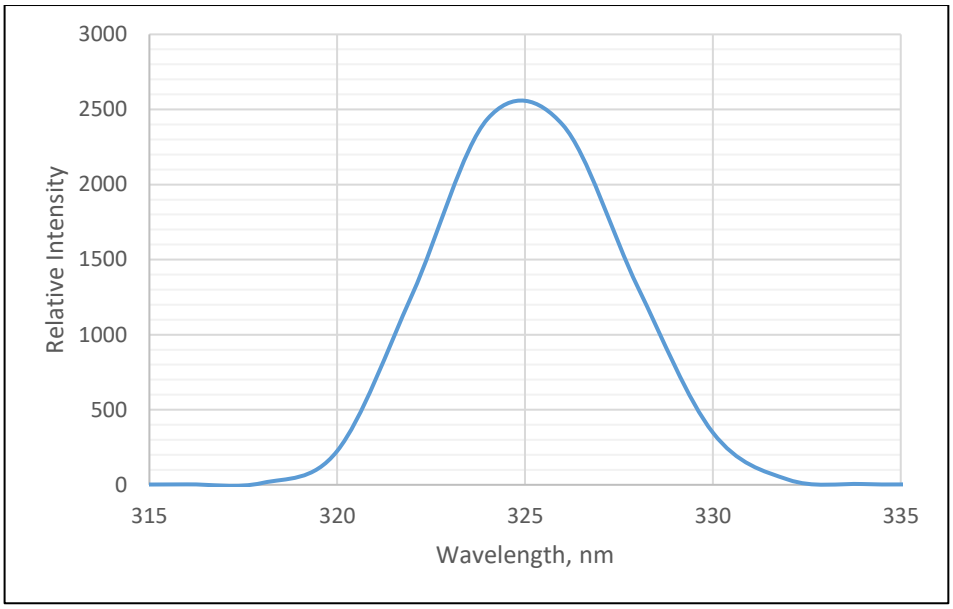

Figure 3.7. Excitation spectrum of TGA-ZnS NPs in neutral medium, pH~7

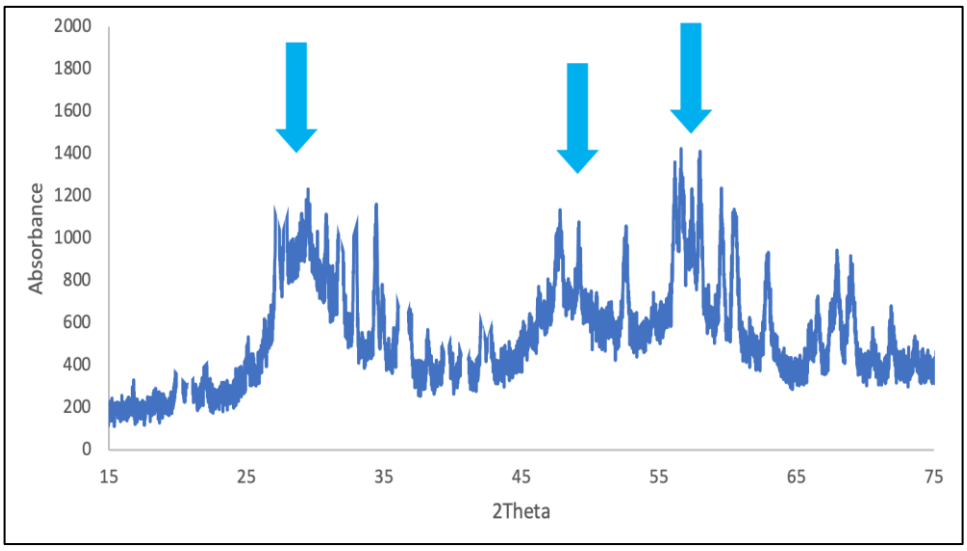

Figure 3.8. XRD spectrum of TGA-ZnS NPs

The XRD spectrum of TGA-ZnS NPs was also taken for further characterization as shown in Figure 3.8. The peaks at 2Theta 29^{o}, 47^{o}, 57^{o} are the characteristic ZnS

peaks [66]. As a result, the XRD pattern indicates that the phase structure of TGA-ZnS NPs can be indexed as cubic zinc blend.

3.2 Analysis of Thiourea-ZnS NPs

Thiourea capped and functionalized ZnS nanoparticles were synthesized in a spherical shape. The amine group (-NH_2) on the surface of the nanoparticles provides stabilization in water. The spherical shape of the Thiourea-ZnS NPs can be seen from transmission electron microscope (TEM) images in Figure 3.9. Also, the dimater of smaller particles is shown in Figure 3.10.

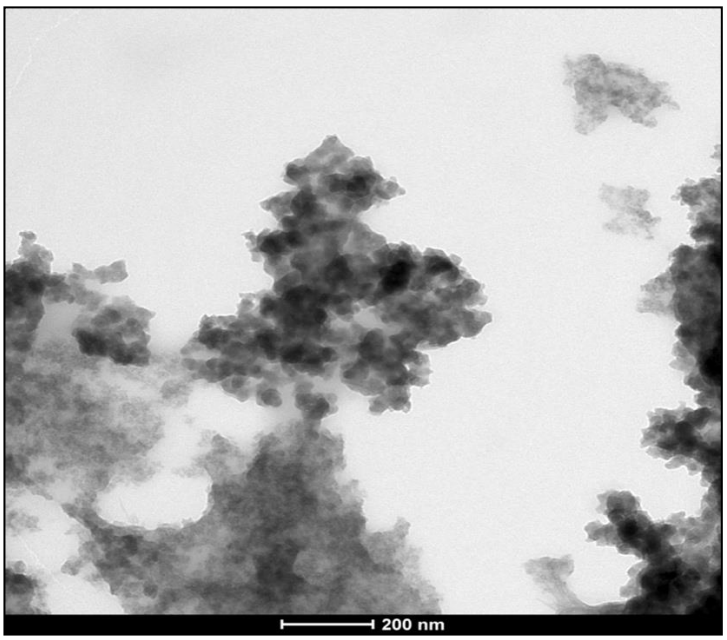

Figure 3.9. TEM image of Thiourea-ZnS NPs prepared in neutral medium, pH~7

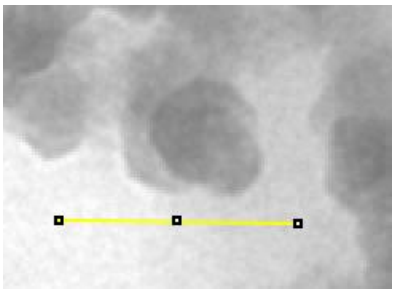

Figure 3.10. TEM image of Thiourea-ZnS NPs prepared in 10 nm scale as shown with yellow color

The diameter distribution graph of Thiourea-ZnS NPs is given in Figure 3.11. The size distribution graph of the spherical-shaped Thiourea-ZnS NPs represents an approximate value of the nanoparticle diameter due to the agglomeration. From the graph, the approximate diameter of the nanoparticles varies between 28-36 nm, and the plateau region of the weighted size distribution graph corresponds to the size distribution of 32-36 nm. The mathematical mean diameter of the particles was calculated as 30 ± 5 nm.

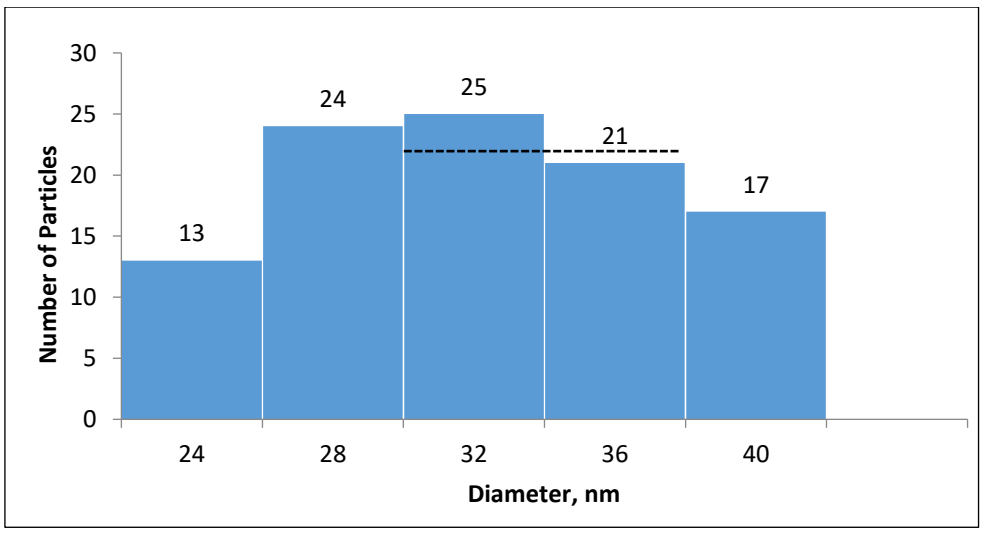

Figure 3.11. Size distribution graph of Thiourea-ZnS nanoparticles

FTIR spectrum of the Thiourea-ZnS NPs were taken to characterize the nanoparticles further. In Figure 3.12, the FTIR spectrum of the Thiourea-ZnS NPs and thiourea is shown [70]. The peaks shown with red arrow are related with thiourea and the peaks shown with blue arrow are related with ZnS. The peaks at 3384 and 3186 cm^{-1} represent the N-H stretching. The peak at 1616 cm^{-1} indicates the N-H bending. The peak at 1388 cm^{-1} and 1117 cm^{-1} represents the C-N asymmetric and symmetric stretching, respectively. The peak at 647 cm^{-1} represents the C=S stretching. Lastly, the peaks at 536 and 465 cm^{-1} indicate the vibrational characteristics of ZnS stretching. The appearance of these peaks indicates the presence of amine groups on the surface of ZnS nanoparticles and the formation of amine functionalized ZnS nanoparticles [65], [66], [70].

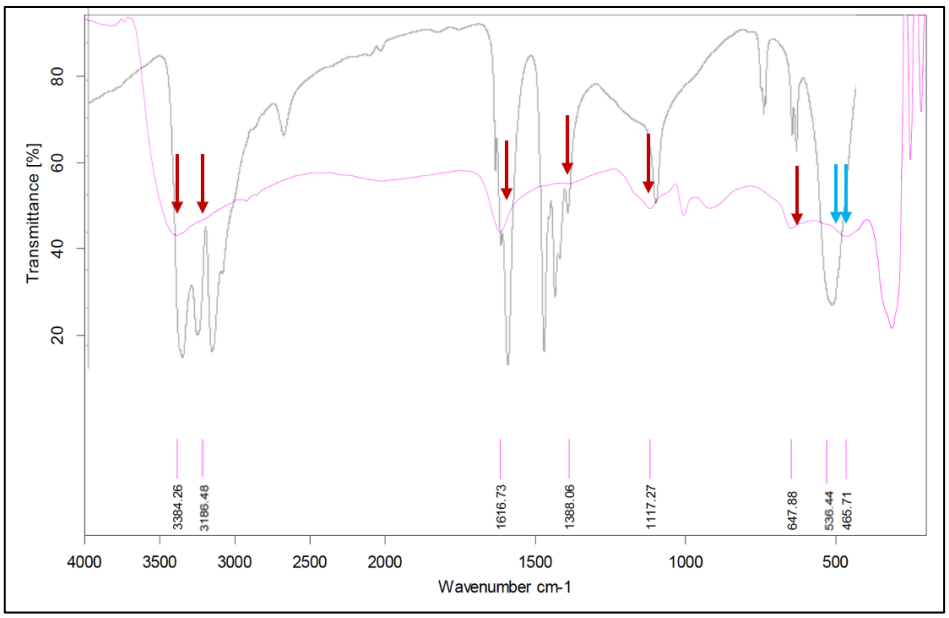

Figure 3.12. FTIR spectrum of Thiourea-ZnS NPs (pink) and thiourea (black)

As shown in Figure 3.13, the nanoparticles exhibit a fluorescence emission maximum at 648 nm when excited at 323 nm and a high emission intensity around

2550 RFU. The fluorescence spectrum of Thiourea-ZnS NPs were taken in aqueous solution.

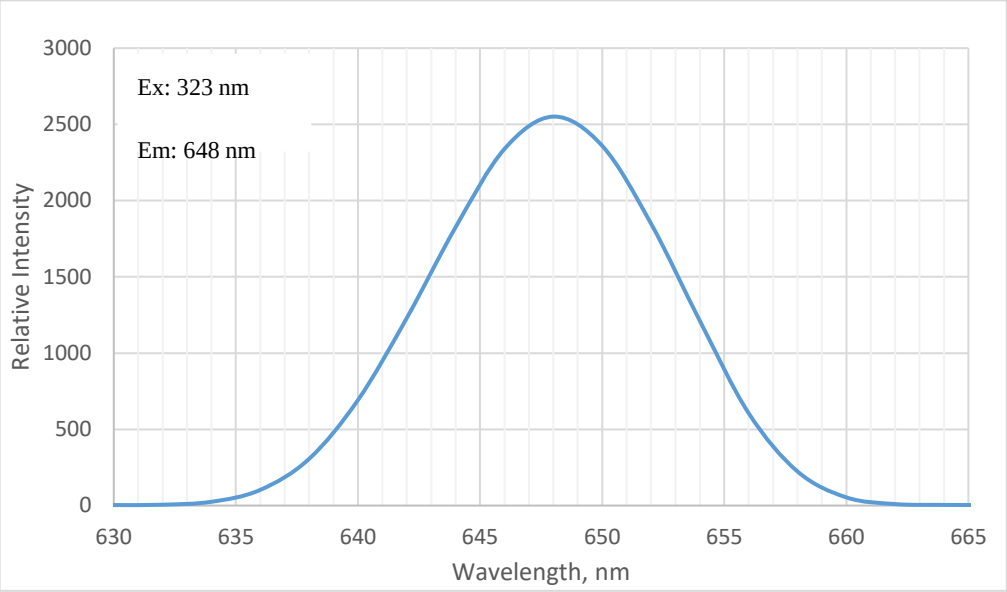

Figure 3.13. Fluorescence spectrum of Thiourea-ZnS NPs in aqueous medium.

3.3 Analysis of TPP-TGA-ZnS NPs

TPP-TGA-ZnS NPs were synthesized by adding TPP to a reaction medium containing DCC, which forms a covalent bond between the -OH group of TPP and the -COOH group of ZnS nanoparticles. TEM image is given in Figure 3.14.

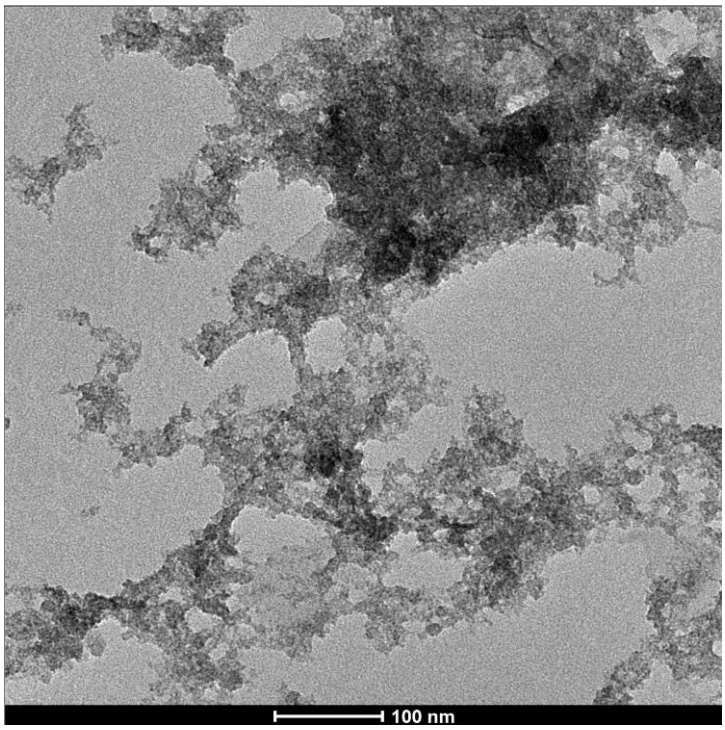

Figure 3.14. TEM image of TPP-TGA-ZnS NPs

The size distribution graph of the TPP-TGA-ZnS NPs represents an approximate value of the nanoparticle diameter due to the agglomeration. From the graph shown in Figure 3.15, the approximate diameter of the nanoparticles varies between 7-11 nm, and the plateau region of the weighted size distribution graph corresponds to the size distribution of 9-11 nm. The mathematical mean diameter of the particles was calculated as 8 ± 2 nm.

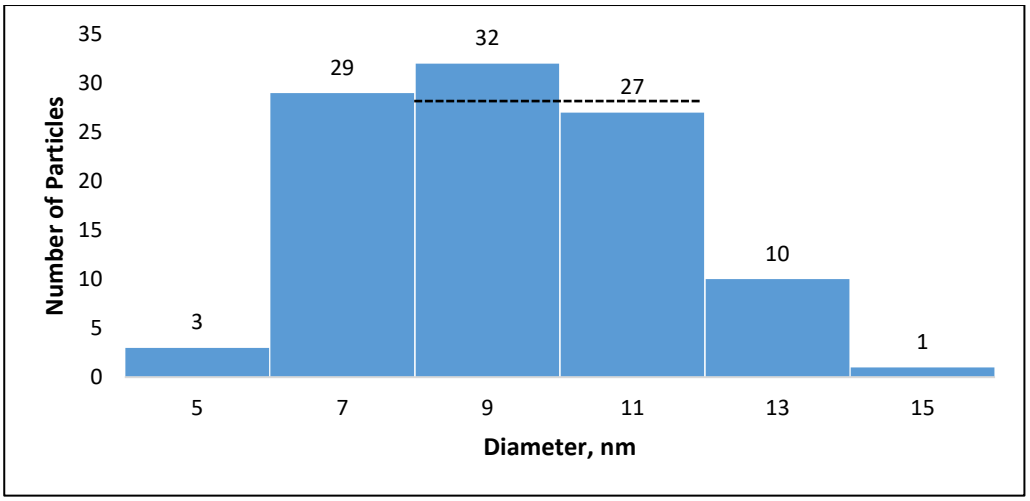

Figure 3.15. Size distribution graph of TPP-TGA-ZnS NPs

In Figure 3.16, the FTIR spectrum of TGA-ZnS NPs (blue) and TPP-TGA-ZnS NPs (red) are given to compare the two nanoparticles with different fucntional groups for further charecterization. The peak at 1741 cm^{-1} which represents C=O stretching. Also, the peaks at 1217, 1155, 1088 and 1034 cm^{-1} represent C-O stretching of the ester bond formed between -COOH group of ZnS nanoparticles and the -OH group of TPP. The peak at 1399 indicates C-C stretching in phenyl ring of TPP. The peak at 1461 cm^{-1} represents the Ph-P bonding. The peak at 408 cm^{-1} which is corresponding to the P-C bond. The presence of these peaks indicates that TPP-TGA-ZnS NPs were synthesized successfully.

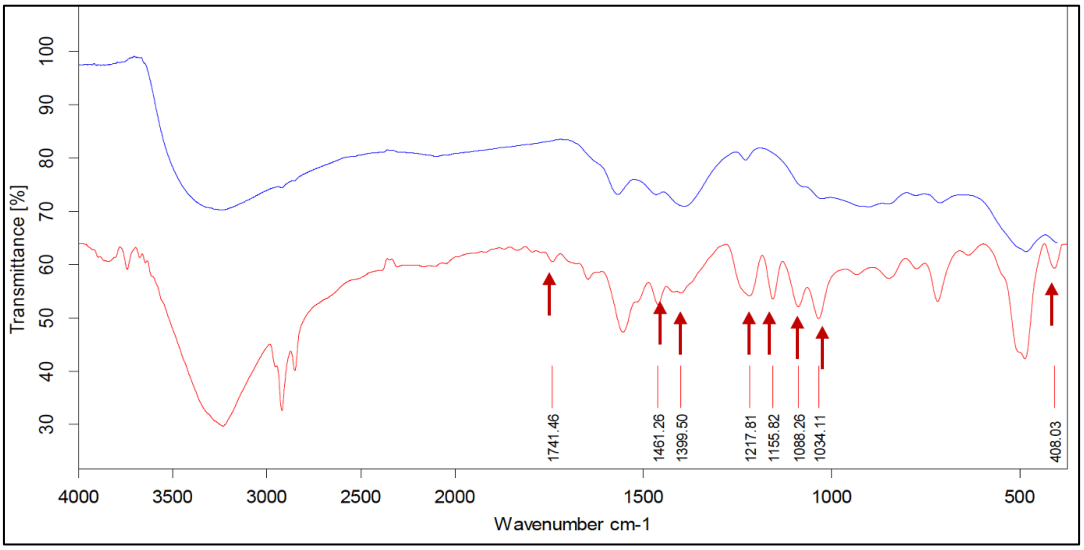

Figure 3.16. FTIR spectrum of TGA-ZnS NPs (blue) and TPP-TGA-ZnS NPs (red)

In Figure 3.17, the fluorescence emission spectrum of TPP-TGA-ZnS NPs is given. The nanoparticles exhibit a fluorescence emission maximum at 650 nm when excited at 320 nm and a high emission intensity around 2700 RFU. 5 nm excitation and emission bandwidth were used.

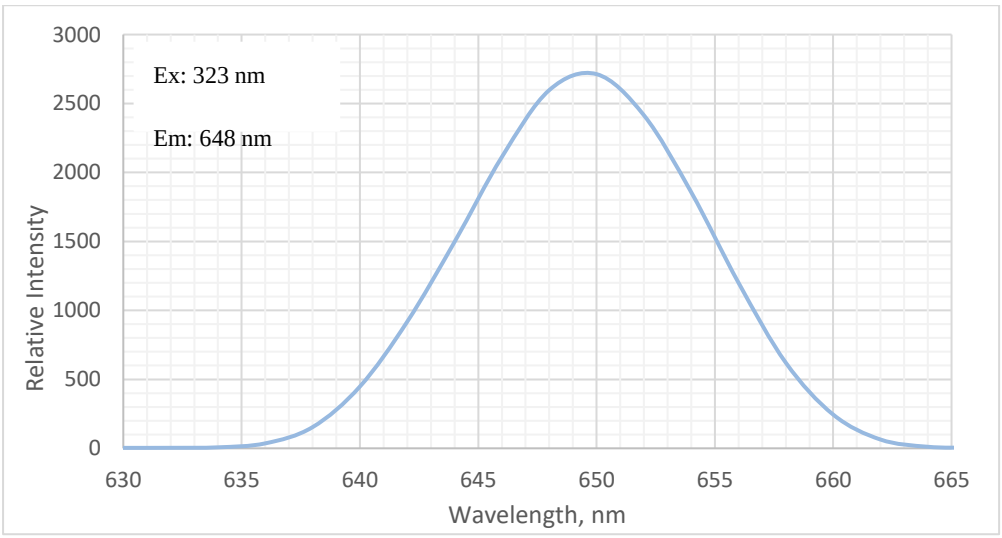

Figure 3.17. Fluorescence spectrum of TPP-TGA-ZnS NPs in aqeuous medium

3.4 Analysis of TPP-Thiourea-ZnS nanoparticles

TPP-Thiourea-ZnS nanoparticles were synthesized by the EDC coupling between the -NH_2 groups of thiourea and the -COOH groups of TPP. The TEM image can be seen in Figure 3.18.

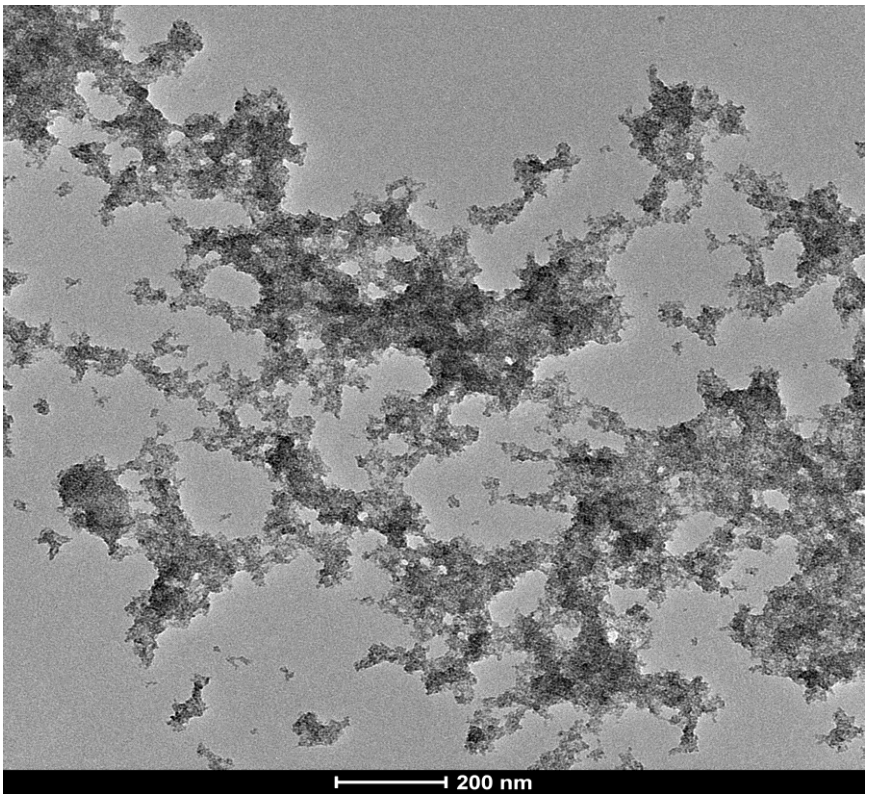

Figure 3.18. TEM image of TPP-Thiourea-ZnS NPs

The size distribution graph of the TPP-Thiourea-ZnS NPs represents an approximate value of the nanoparticle diameter due to the agglomeration. From the graph shown in Figure 3.19, the approximate diameter of the nanoparticles varies between 4-5 nm with a peak point at 5 nm. The mathematical mean diameter of the particles was calculated as 4.5 ± 1.0 nm.

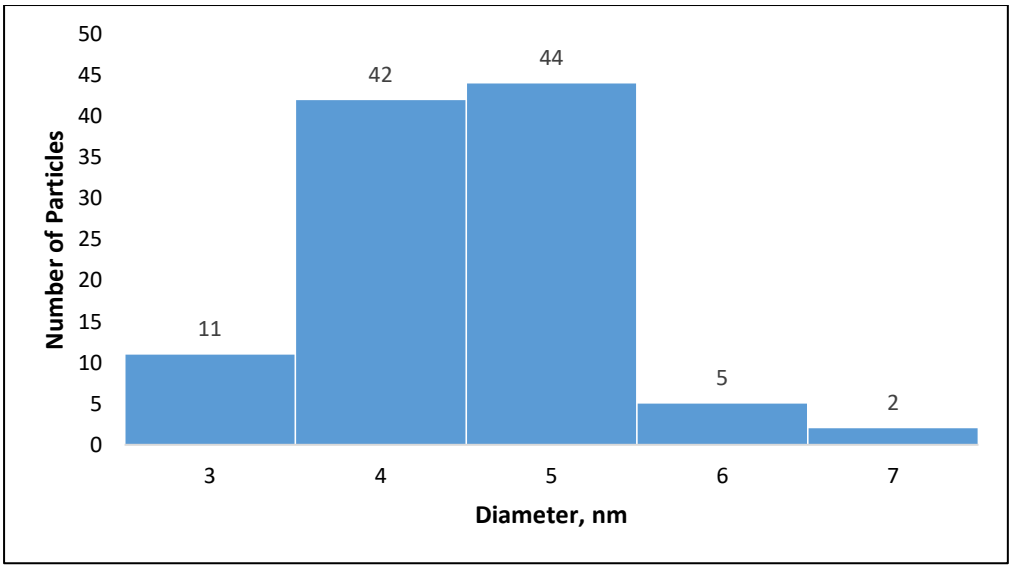

Figure 3.19. Size distribution graph of TPP-Thiourea-ZnS NPs

The FTIR spectra of Thiourea-ZnS NPs and TPP-Thiourea-ZnS NPs were compared in order to determine the different fuctional groups present in both coated and noncoated nanoparticles as shown in Figure 3.20. The peak at 1677 cm^{-1} represents the secondary amide bond formed between the -NH_2 group of Thiourea-ZnS NPs and the -COOH group of TPP. The peak at 1457 cm^{-1} represents the Ph-P bonding of TPP. The peak at 1399 cm^{-1} indicates C-C stretching in phenyl ring of TPP. The peak at 997 cm^{-1} represents the C-H bending of TPP. The peak appeared at 421 cm^{-1} is related to P-C bond of the TPP. The appearance of these peaks indicates the presence of TPP group on the surface of ZnS nanoparticles and the formation of TPP-Thiourea-ZnS NPs.

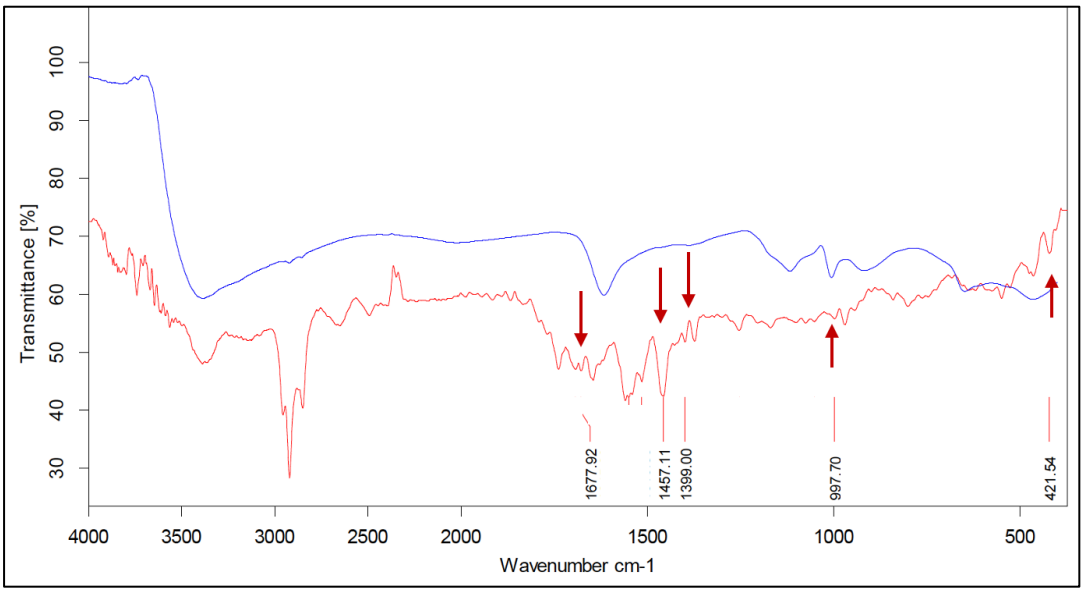

Figure 3.20. FTIR spectra of Thiourea-ZnS NPs (blue) and TPP-Thiourea-ZnS NPs (red)

In Figure 3.21, the fluorescence spectrum of TPP-Thiourea-ZnS NPs is given. The nanoparticles exhibit a fluorescence maximum at 650 nm when excited at 323 nm and a high emission intensity around 1715 RFU. 5 nm excitation and emission bandwidth were used.

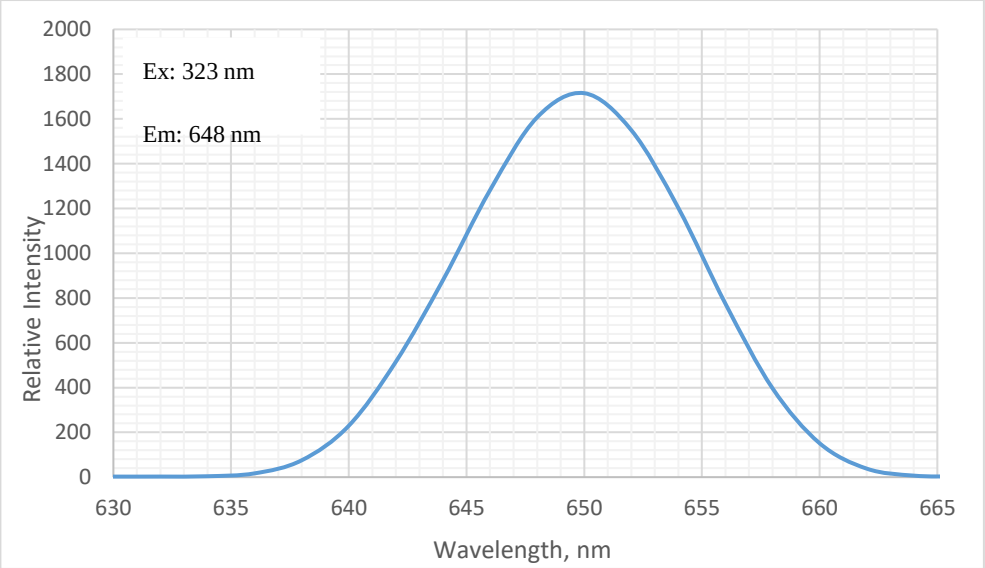

Figure 3.21. Fluorescence spectrum of TPP-Thiourea-ZnS NPs in aqueous medium

3.5 Optimization Studies for the Synthesized ZnS NPs

3.5.1 Zeta Size and Potential Measurements

In order to determine the hydrodynamic radius and surface charge of the TGA-ZnS NPs, Thiourea-ZnS NPs, TPP-TGA-ZnS NPs and TPP-Thiourea-ZnS NPs, zeta size and potential measurements were obtained. The zeta size of the synthesized ZnS nanoparticles provides information about their agglomerated size.

Also, zeta potential of the synthesized ZnS nanoparticles was measured to confirm the surface functionalization.

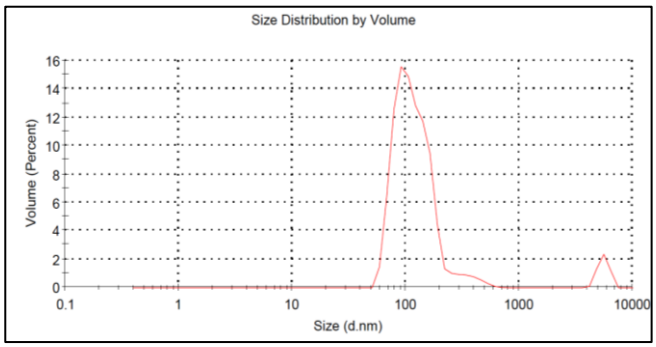

Figure 3.22. Zeta size graph of TGA-ZnS NPs

The zeta size graph of TGA-ZnS NPs is given in Figure 3.22. According to the graph, the zeta size of the TGA-ZnS NPs were measured as 127 nm. This result was also in correlation with the TEM image of TGA-ZnS NPs (0.64 mmol of TGA).

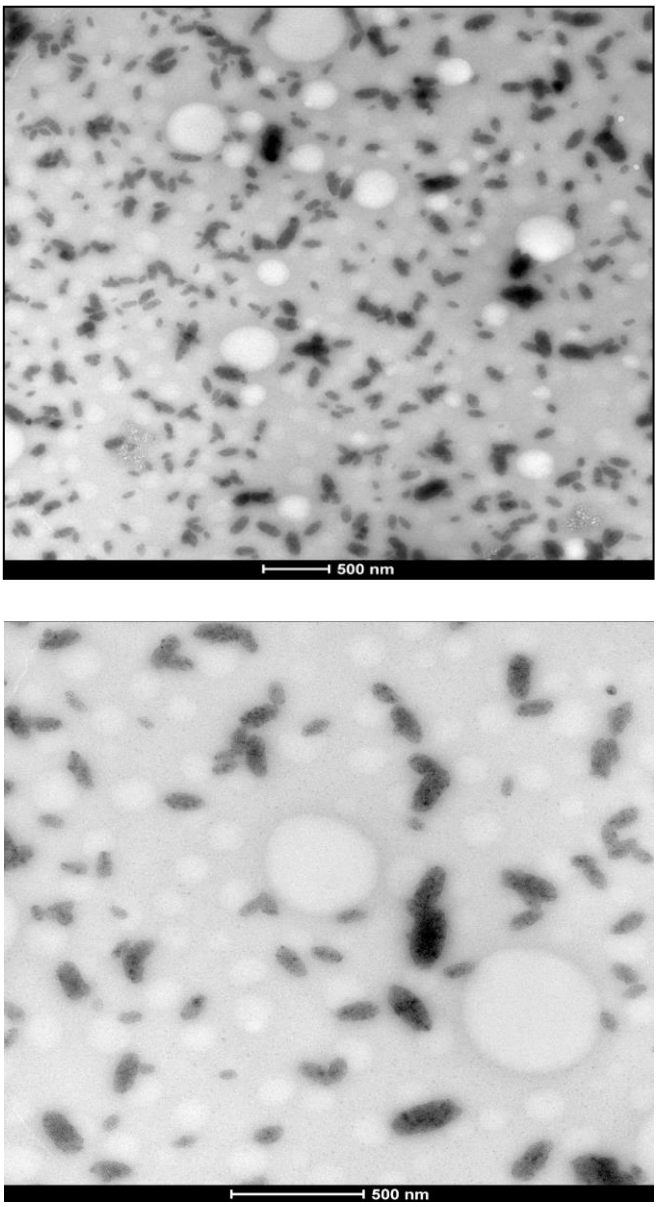

Figure 3.23. TEM images of TGA-ZnS NPs

As can be seen from the TEM image in Figure 3.23, the dimensions of large agglomerates and individual capsule shape particles are around 200 nm and 125 nm respectively. After they were coated with the TPP, their average hydrodynamic size was measured as 270 nm. Also, the surface potential of TGA-ZnS NPs was measured as -31.3 mV initially. The negative potential on the surface of these nanoparticles

indicates the presence of negatively charged -COO^- groups. After coated with TPP cation, the surface charge of TPP-TGA-ZnS NPs became -8.5 mV. It was expected that the positive charge on the phosphorous group of TPP would neutralize some of the negative charge on the surface of the TGA-ZnS NPs. The increase of zeta potential in the positive direction indicates that the surface of TGA-ZnS NPs were coated with TPP cation. The increase in the size of the TPP-TGA-ZnS NPs was correlated with the decreasing negative surface charge. When the surface charge decreases, the electrostatic repulsive forces between TPP-TGA-ZnS NPs decrease, leading agglomeration.

Moreover, the average hydrodynamic size of Thiourea-ZnS NPs were measured as 146 nm. As they were coated with TPP, their average zeta size became 970 nm. Also, the surface potential of Thiourea-ZnS NPs was measured as -3.7 mV. The surface charge of these nanoparticles was almost neutral due to the presence of -NH_2 groups on the surface. When they were coated with TPP cation, the surface charge becomes more positive, indicating the presence of the positively charged TPP cation on the surface. Although there was not a significant change in their surface charge, the hydrodynamic size of these nanoparticles changed drastically. It was concluded that the colloidal stability of TPP-Thiourea-ZnS NPs was low, and interparticle interactions were high [67]. A drastic change in the synthesis process was required in order to reduce the agglomeration size of TPP-Thiourea-ZnS NPs. When both TGA-ZnS and Thiourea-ZnS NPs coated with TPP, it was observed that the increase in the zeta potential of TPP-TGA-ZnS NPs were higher compared to the TPP-Thiourea-ZnS NPs. Probably the coating efficiency of TGA-ZnS NPs was higher than that of Thiourea-ZnS NPs. Therefore, we decided to focus only on reducing aggregate sizes of TGA-ZnS nanoparticles for further studies. In Table 3.1, zeta size and potential measurements of TGA-ZnS NPs, Thiourea-ZnS NPs, TPP-TGA-ZnS NPs and TPP-Thiourea-ZnS NPs were summarized.

Table 3.1. Zeta Size and Potential of TGA-ZnS NPs, Thiourea-ZnS NPs, TPP-TGA-ZnS NPs and TPP-Thiourea-ZnS NPs

	Zeta Size, nm (mean)	**Zeta Potential, mV (mean)**
TGA-ZnS NPs	127	-31.3
Thiourea-ZnS NPs	146	-3.7
TPP-TGA-ZnS NPs	270	-8.5
TPP-Thiourea-ZnS NPs	970	1.1

3.5.2 Optimization of the Size of TGA-ZnS NPs

It was aimed to optimize the size of the TGA-ZnS NPs to obtain a smaller particle size so that they would be more compatible with the sizes of cell structure and promote cellular uptake. In order to decrease the particles size compared to the TGA-ZnS (0.64 mmol TGA), a bulky capping agent such as 11-Mercaptoundecanoic acid (MUA) was used. Figure 3.24 shows the zeta size graph of MUA capped ZnS NPs (MUA-ZnS NPs).

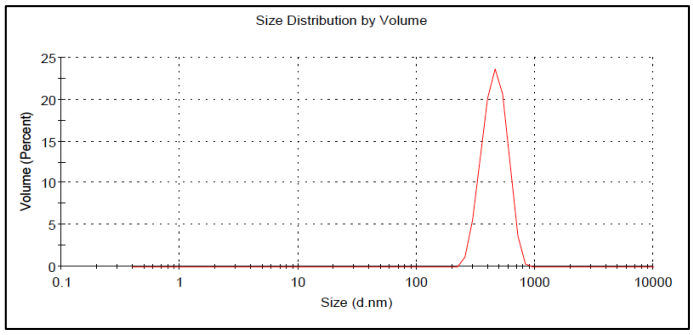

Figure 3.24. Zeta size graph of MUA-ZnS NPs

The zeta size and potential measurements of MUA-ZnS NPs were also given in Table 3.2. Since the zeta size of the ZnS NPs were not decreased, the optimization studies on MUA-ZnS NPs were not continued.

Table 3.2. Zeta Size and Potential of MUA-ZnS NPs

	Zeta Size, nm (mean)	**Zeta Potential, mV (mean)**
MUA-ZnS NPs	464	-24.1

It was expected that agglomeration of the nanoparticles could be prevented by increasing the surface charge when the amount of capping agent is increased. Also, it was expected that decreasing the centrifugation time during the washing process would prevent the agglomeration. For this purpose, TGA-ZnS NPs were prepared by increasing the amount of TGA for two and four times, and the centrifugation time decreased. The results are displayed in Figure 3.25. In Table 3.3, the changes in the size and potential of the TGA-ZnS NPs were given when 1.28 and 2.58 mmol of TGA was used in the synthesis of the particles.

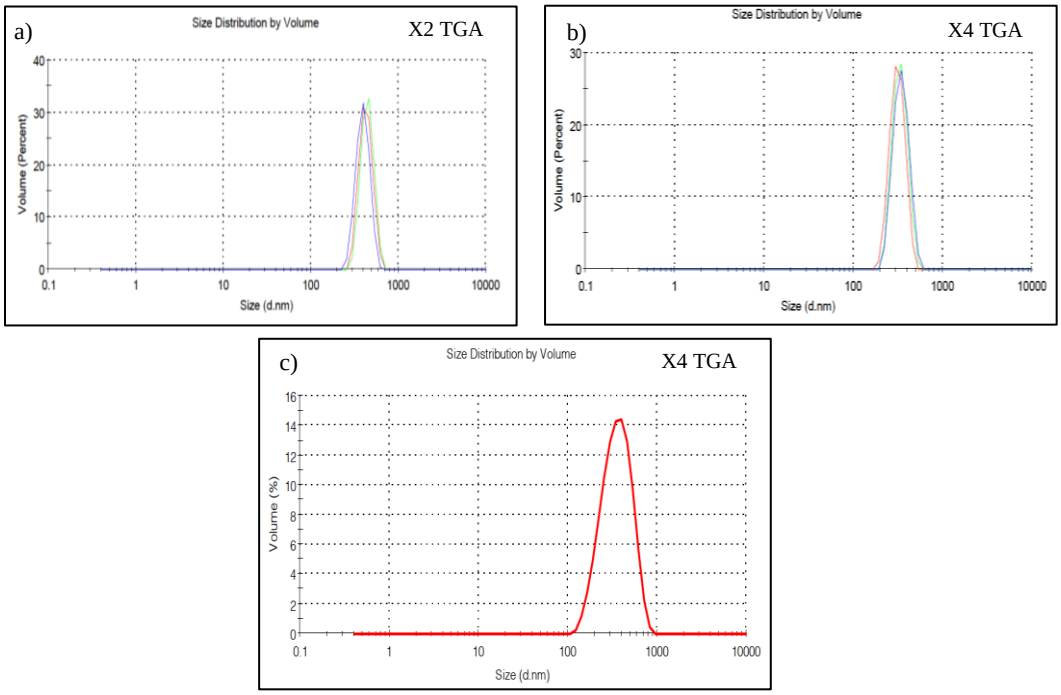

Figure 3.25. Zeta size graphs of a) TGA-ZnS NPs (1.28 mmol of TGA), b) TGA-ZnS NPs (2.58 mmol of TGA), and c) TGA-ZnS NPs (2.58 mmol of TGA, supernatant)

The size of TGA-ZnS NPs was expected to decrease as the amount of capping agent increased due to the increase in their surface potential in the negative direction. In addition, the centrifugation time was shortened. However, as shown in Figure 3.25, the size of the TGA-ZnS NPs increases and reaches a constant size distribution when 1.28 and 2.58 mmol of TGA was used. This behavior can be explained by the interaction of the carboxylate groups with the Zn ions which decreases the repulsive forces between TGA-ZnS NPs, leading agglomeration [68].

The supernatant of the TGA-ZnS NPs (2.58 mmol of TGA) solution was also analyzed in order to measure the size and potential of non-precipitated TGA-ZnS NPs after centrifugation at 5000 rpm for five minutes. As seen in Table 3.3, the size of TGA-ZnS NPs (2.58 mmol of TGA), suspended in the supernatant was larger compared to those that precipitated, indicating the presence of another type of

agglomerate with lower density. TGA is one of the thiol-containing metal chelating agents. Therefore, this secondary aggregate formation is probably due to the formation of the Zn-TGA complex in the presence of excess TGA [69].

Table 3.3. Zeta Size and Potential of TGA-ZnS NPs (0.64 mmol of TGA), TGA-ZnS NPs (1.28 mmol of TGA), TGA-ZnS NPs (2.58 mmol of TGA), TGA-ZnS NPs (2.58 mmol of TGA, supernatant) in neutral medium, pH~7

The number of mmol of TGA used in the synthesis of TGA-ZnS NPs	**Zeta Size, nm (mean)**	**Zeta Potential, mV (mean)**	**Centrifugation Procedure**
TGA-ZnS NPs (0.64 mmol of TGA)	127	-31.3	5000 rpm for 20 min
TGA-ZnS NPs (1.28 mmol of TGA)	411	-24.8	5000 rpm for 5 min
TGA-ZnS NPs (2.58 mmol of TGA)	333	-46.4	5000 rpm for 5 min
TGA-ZnS NPs (2.58 mmol of TGA)	370	-19.3	5000 rpm for 3 min, supernatant

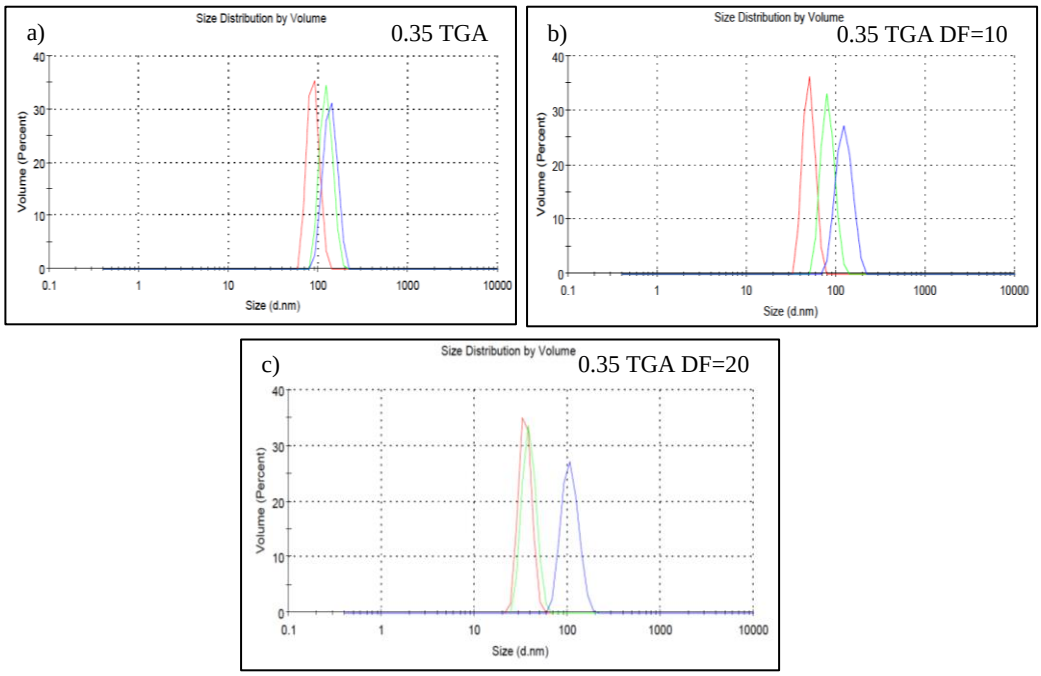

Figure 3.26. Zeta size graphs of a) TGA-ZnS NPs (0.35 mmol of TGA), b) TGA-ZnS NPs (0.35 mmol of TGA, DF=10), and c) TGA-ZnS NPs (0.35 mmol of TGA, DF=20)

As a result of the zeta size and potential measurements, it was aimed to reduce the amount of capping agent, considering that using a smaller amount of capping agent could reduce the complex formation effect and the size of the nanoparticles. For this purpose, the amount of TGA was reduced by almost half. After synthesizing TGA-ZnS NPs (0.35 mmol TGA), they were centrifuged at 5000 rpm for 15 mins at pH 12.0. Since it was observed that the synthesized TGA-ZnS NPs did not form agglomerates at pH 12.0, the nanoparticle solution was washed in alkaline medium [74]. Also, the effect of the dilution on the size and the surface charge of TGA-ZnS NPs were analyzed by Zetasizer. The results are presented in Figure 3.26 and Table 3.4.

As shown in Figure 3.26, the size of the TGA-ZnS NPs were 117 nm when they were centrifuged and washed at pH 12. There was a decrease in the size of the TGA-ZnS

NPs compared to the centrifugation in neutral medium due to the colloidal stability of these nanoparticles at pH 12.0. This result can also be correlated with the increase in the surface potential of TGA-ZnS NPs being -52.4 mV. to the higher negative charge on the surface of the TGA-ZnS NPs, they tend to agglomerate less.

Moreover, when the TGA-ZnS NPs were diluted with a dilution factor of 10 and 20, their zeta size decreased as a result of a more uniform distribution in dilute solutions.

Table 3.4. Zeta Size and Potential of TGA-ZnS NPs centrifuged at pH 12, diluted with DF of 10 and 20

The number of mmol of TGA used in the synthesis of TGA-ZnS NPs	**Zeta Size, nm (mean)**	**Zeta Potential, mV (mean)**	**Centrifugation Procedure**
TGA-ZnS NPs (0.35 mmol of TGA)	117	-52.4	5000 rpm for 15 min, at pH 12
TGA-ZnS NPs (0.35 mmol of TGA)	86	-42.9	5000 rpm for 15 min, at pH 12 DF = 10
TGA-ZnS NPs (0.35 mmol of TGA)	61	-32.6	5000 rpm for 15 min, at pH 12 DF = 20

3.5.2.1 The Effect of the Amount Capping Agent on The Fluorescent Properties of TGA-ZnS NPs

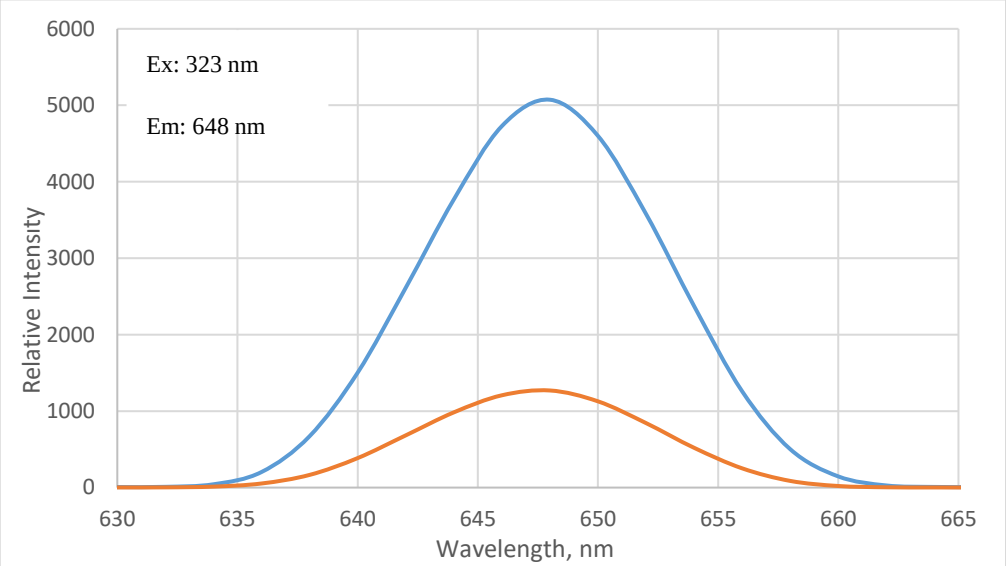

Figure 3.27. Fluorescence spectrum of TGA-ZnS NPs (0.64 mmol of TGA, red) and TGA-ZnS NPs (0.35 mmol of TGA, blue)

As shown in Figure 3.27, the relative fluorescence emission intensity of TGA-ZnS NPs was increased by almost 5 times when 0.35 mmol of TGA was used. 5 nm excitation and emission bandwidth were used during the measurement. This result shows that the reduction in the amount of TGA used probably diminishes the quenching effect of TGA on the fluorescence emission of the particles in addition to the reduction of agglomerate sizes.

3.5.3 Zeta Size and Potential of TPP-TGA-ZnS NPs

As a result of these zeta size and potential measurements, decreasing the amount of capping agent and centrifuging the nanoparticles in alkaline medium yielded smaller size of TGA-ZnS NPs. Therefore, TPP-TGA-ZnS NPs were synthesized by using TGA-ZnS NPs (0.35 mmol of TGA), and their zeta size and potential were measured

as 273 nm and -18.0 mV respectively. The zeta size graph and the measurement data are given in Figure 3.28 and Table 3.5 respectively.

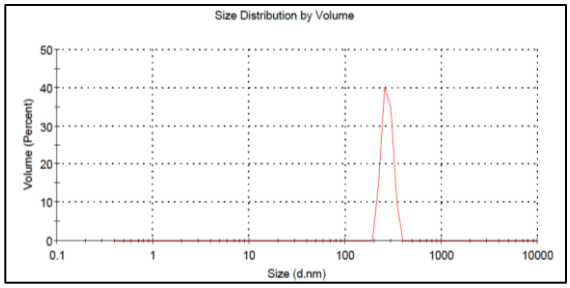

Figure 3.28. Zeta size graph of TPP-TGA-ZnS NPs (0.35 mmol of TGA)

It was expected that after coated with TPP, the positive charge on the surface of TPP cation would neutralize some of the negative charge on the surface of TGA-ZnS NPs. The increase of zeta potential in the positive direction indicates that the surface of TGA-ZnS NPs were coated with TPP cation. The increase in the size of the TPP-TGA-ZnS NPs was correlated with the decreasing negative surface charge. When the surface charge decreases, the electrostatic repulsive forces between TPP-TGA-ZnS NPs decrease, leading agglomeration.

Table 3.5. Zeta Size and Potential of TPP-TGA-ZnS NPs

	Zeta Size, nm (mean)	**Zeta Potential, mV (mean)**	**Centrifugation Procedure**
TPP-TGA-ZnS NPs (0.35 mmol of TGA)	273	-18.0	5000 rpm for 15 min, at pH 12

3.5.4 Zeta Size and Potential of Glu-Hep-TPP-TGA-ZnS NPs

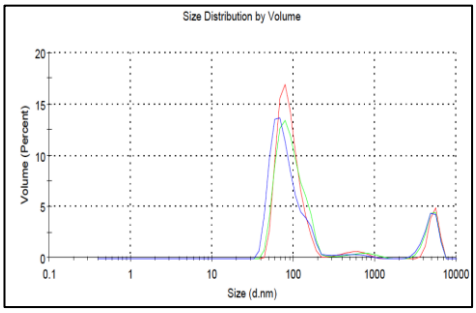

Figure 3.29. Zeta size graph of Glu-Hep-TPP-TGA-ZnS NPs (0.35 mmol of TGA)

As shown in the Table 3.6, when the surface potential of TPP-TGA-ZnS NPs and Hep-TPP-TGA-ZnS NPs were compared, due to the negative charge of heparin, the surface charge of Hep-TPP-TGA-ZnS NPs increased in the negative direction approximately 1.5 times and became -27.3. Also, the higher negative surface potential on the Hep-TPP-TGA-ZnS NPs prevent the agglomeration of Hep-TPP-TGA-ZnS NPs, and a decrease in the zeta size was observed.

When the surface potential of Hep-TPP-TGA-ZnS NPs and Glu-Hep-TPP-TGA-ZnS NPs were compared, since some of the negative charge due to heparin was neutralized owing to the covalent bond formation of glucose through the acid groups of heparin, a decrease in the surface charge on Glu-Hep-TPP-TGA-ZnS NPs was observed. There was not a significant change in the zeta size of Glu-Hep-TPP-TGA-ZnS NPs compared to Hep-TPP-TGA-ZnS NPs. The zeta size graph of Glu-Hep-TPP-TGA-ZnS NPs is given in Figure 3.29.

Table 3.6. Zeta Size and Potential of Hep-TPP-TGA-ZnS NPs and Glu-Hep-TPP-TGA-ZnS NPs

	Zeta Size, nm (mean)	**Zeta Potential, mV (mean)**	**Centrifugation Procedure**
Hep-TPP-TGA-ZnS NPs (0.35 mmol of TGA)	86	-27.3	13.500 rpm, multiple times
Glu-Hep-TPP-TGA-ZnS NPs (0.35 mmol of TGA)	67	-14.5	13.500 rpm, multiple times

3.5.4.1 The Fluorescent Properties of Glu-Hep-TPP-TGA-ZnS NPs

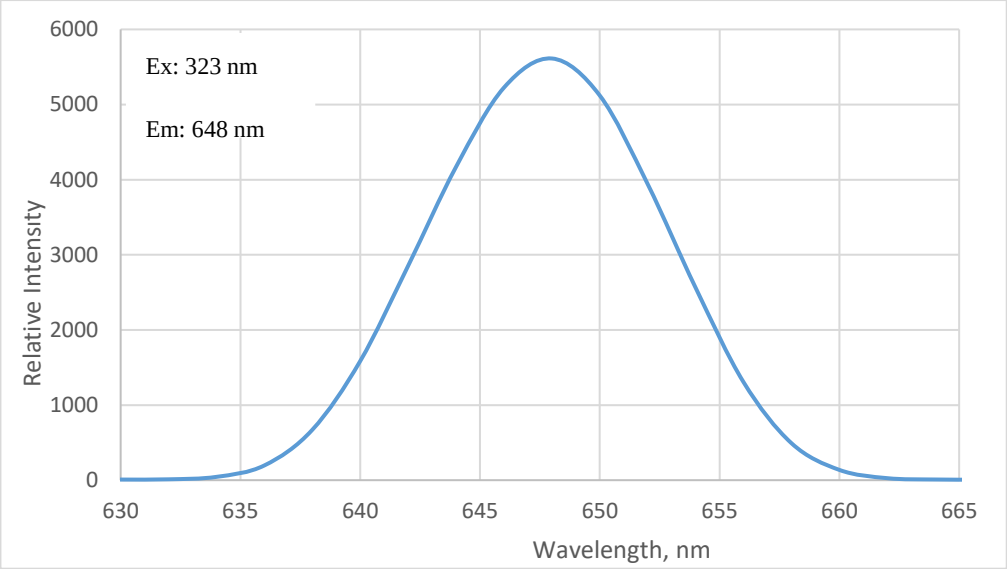

Figure 3.30. Fluorescence spectrum of Glu-Hep-TPP-TGA-ZnS NPs

In Figure 3.30, the fluorescence emission spectrum of Hep-TPP-TGA-ZnS NPs is given. The nanoparticles exhibit a fluorescence emission maximum at 648 nm when excited at 323 nm and a high emission intensity around 5600 RFU. 5 nm excitation and emission bandwidth were used.

3.6 Intracellular Analysis

Glu-Hep-TPP-TGA-ZnS NPs and Glu-TPP-TGA-ZnS NPs were used in the measurements. 120 µg/mL of these nanoparticles were prepared and dispersed in deionized water. They were added into the N2a cell lines and incubated for 5 h. After the incubation time was over, the bright field images and the fluorescence images of the N2a cells were taken as shown in Figure 3.31.

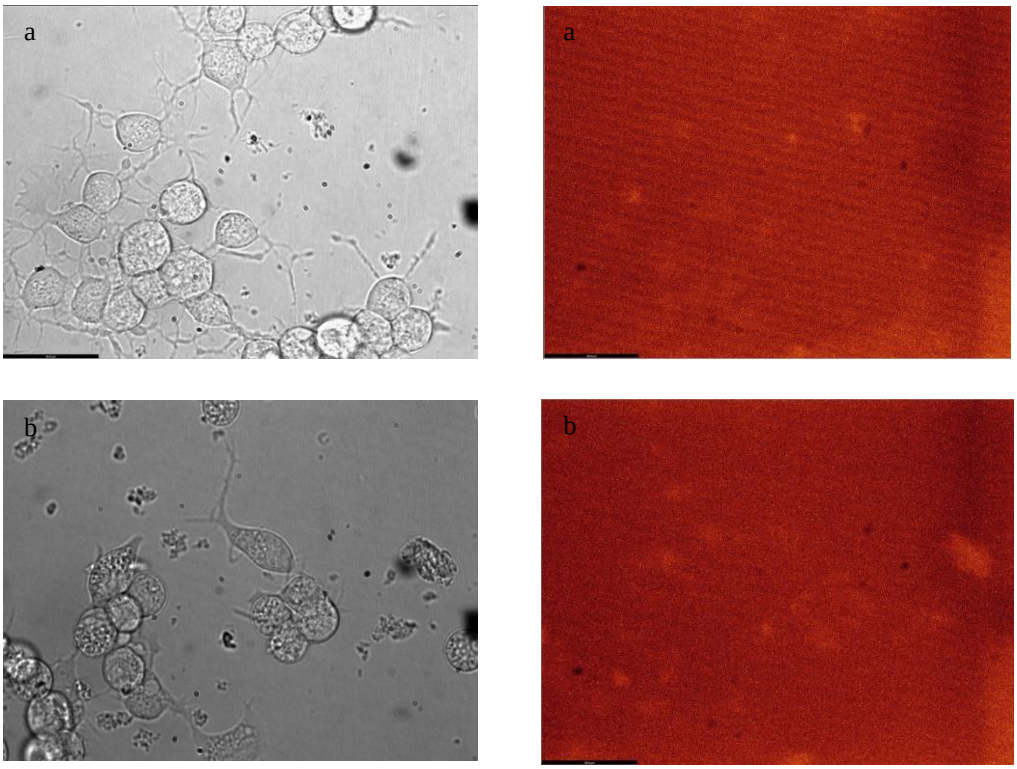

Figure 3.31. Bright filed and fluorescence images of N2a cells after the addition of a) Glu-Hep-TPP-TGA-ZnS NPs, b) Glu-TPP-TGA-ZnS NPs

Since the maximum excitation wavelength that could be used by fluorescence microscope and the excitation maximum of the nanoparticles were not overlapping, the fluorescence of nanoparticles incubated in the cell lines could not be observed. Although the fluorescence imaging of the cell lines was not realized, the outcomes of these studies have shown that Glu-Hep-TPP-TGA-ZnS NPs and Glu-TPP-TGA-ZnS NPs were not toxic towards N2a cells. For mitochondrial imaging applications, the studies are in progress.

CHAPTER 4

CONCLUSION

Fluorescent imaging probes provides high resolution, sensitivity, and selectivity for the mitochondria imaging of cancer cells. Among the semicondutor fluorescent nanoparticles, ZnS nanoparticles are used in biomedical applications due to their high fluorescence intensity and low toxicity. Therefore, the aim of the study is to synthesize surface functionalized zinc sulfide semiconductor nanoparticles for mitochondria imaging of cancer cells.

The interaction of capping agents with the surface of the nanoparticles plays a crucial role forthe stabilization of the nanoparticles. Also, the size and morphology of nanoparticles can be altered by using proper capping agents.

Initially, ZnS nanoparticles were synthesized by using TGA and thiourea as capping agents. TGA-ZnS NPs were synthesized by a simple and green method. The avarage height of capsule-shaped TGA-ZnS NPs were 92 ± 6 nm, and the average width of TGA-ZnS NPs were 52 ± 5 nm. The surface functionalization of TGA-ZnS NPs was confirmed by FTIR measurements. Also, TGA-ZnS NPs exhibit high fluorescent emission maximum at 648 nm with an intensity of 1270 RFU when excited at 323 nm.

Then, Thiourea-ZnS NPs were synthesized by using another s-terminated capping agent, thiourea. The average diameter of spherical-shaped Thiourea-ZnS NPs was 30 ± 5 nm which was obtained from TEM images. The surface functionalization of Thiourea-ZnS NPs was confirmed by FTIR measurements. Also, Thiourea-ZnS NPs exhibit high fluorescent emission maximum at 648 nm with an emission intensity of 2550 RFU when excited at 323 nm.

TPP cation was used as mitochondria targeting moiety due to its low reactivity inside cells, easy synthesis, and purification. TGA-ZnS NPs were coated with TPP by a

carbodiimide reaction with DCC. Since TPP-TGA-ZnS NPs were agglomarated, only an approximate dimater could be determined. The avarage approximate diamater of TPP-TGA-ZnS NPs were measured as 8 ± 2 nm from TEM images. The FTIR spectra of TGA-ZnS NPs and TPP-TGA-ZnS NPs were compared in order to observe the formation of new peaks due to presence of TPP. The formation of TPP-TGA-ZnS NPs was confirmed by FTIR measurements. Also, TPP-TGA-ZnS NPs exhibit a fluorescence emission maximum at 650 nm with an emission intensity of 2700 RFU when excited at 323 nm.

TPP-Thiourea-ZnS nanoparticles were synthesized by the EDC coupling between the -NH_2 groups of Thiourea-ZnS NPs and the -COOH groups of TPP. Due to the agglomeration of TPP-Thiourea-ZnS NPs, only an approximate diameter could be determined. Accoring to the TEM images, the approximate average diameter of the nanoparticles was 4.5 ± 1.0 nm. The formation of TPP-Thiourea-ZnS NPs was confirmed by FTIR measurements which indicates the TPP coating. Moreover, TPP-Thiourea-ZnS NPs exhibit a high emission maximum at 650 nm with an emission intensity of 1715 RFU when excited at 323 nm. The red shift in the fluorescence emission spectrum of the TPP-Thiourea-ZnS NPs indicate the increased diameter due to coating.

Aqueous solutions of nanoparticles are preferred in biological research, however in this environment, nanoparticles usually agglomerate. Therefore, the sizes of the agglomerates of the synthesized nanoparticles are more important than their individual sizes. As a result, zeta sizes and potentials of TGA-ZnS NPs, Thiourea-ZnS NPs, TPP-TGA-ZnS NPs and TPP-Thiourea-ZnS NPs were measured. According to the review data, it was concluded that the colloidal stability TGA-ZnS NPs was higher compared to Thiourea-ZnS NPs. Both TGA-ZnS and Thiourea-ZnS NPs showed an increase in the zeta potential to the positive direction after reacting with TPP, indicating the TPP coating. However, the coating efficiency of TGA-ZnS NPs was higher than that of Thiourea-ZnS NPs.

Also, the size and surface charge of the TGA-ZnS NPs were optimized by changing the reaction procedures and followed by zeta size and potential measurements.

Since the maximum excitation wavelength that could be used by fluorescence microscope and the excitation maximum of the synthesized nanoparticles are different, the nanoparticles did not show any fluorescence intensity. As a result of the studies on intracellular analysis, Glu-Hep-TPP-TGA-ZnS NPs and Glu-TPP-TGA-ZnS NPs exhibited low toxicity towards N2a cells after incubation. For mitochondrial imaging applications, the studies are in progress.

REFERENCES

[1] C. Jianrong, M. Yuqing, H. Nongyue, W. Xiaohua, and L. Sijiao, "Nanotechnology and biosensors," *Biotechnol. Adv.*, vol. 22, no. 7, pp. 505–518, 2004, doi: 10.1016/j.biotechadv.2004.03.004.

[2] F. Sanchezand and K. Sobolev, "Nanotechnology in concrete - A review," *Constr. Build. Mater.*, vol. 24, no. 11, pp. 2060–2071, 2010, doi: 10.1016/j.conbuildmat.2010.03.014.

[3] S. E. McNeil, "Nanotechnology for the biologist," *J. Leukoc. Biol.*, vol. 78, no. 3, pp. 585–594, 2005, doi: 10.1189/jlb.0205074.

[4] C. P. Poole and F. J. Owens, "Introduction to nanotechnology." Hoboken, NJ: J. Wiley, 2003.

[5] V. Biju, T. Itoh, A. Anas, A. Sujith, and M. Ishikawa, "Semiconductor quantum dots and metal nanoparticles: Syntheses, optical properties, and biological applications," *Anal. Bioanal. Chem.*, vol. 391, no. 7, pp. 2469–2495, 2008, doi: 10.1007/s00216-008-2185-7.

[6] N. A. I. Md Ishak, S. K. Kamarudin, and S. N. Timmiati, "Green synthesis of metal and metal oxide nanoparticles via plant extracts: an overview," *Mater. Res. Express*, vol. 6, no. 11, 2019, doi: 10.1088/2053-1591/ab4458.

[7] F. Mohammad and H. A. Al-Lohedan, "Toxicity assessment of engineered Mn–ZnS quantum dots in vitro," *J. Mater. Sci.*, vol. 51, no. 20, pp. 9207–9216, 2016, doi: 10.1007/s10853-016-0149-4.

[8] H. R. Rajabi and M. Farsi, "Study of capping agent effect on the structural, optical and photocatalytic properties of zinc sulfide quantum dots," *Mater. Sci. Semicond. Process.*, vol. 48, pp. 14–22, 2016, doi: 10.1016/j.mssp.2016.02.021.

[9] Y. Wangand and L. Chen, "Quantum dots, lighting up the research and development of nanomedicine," *Nanomedicine Nanotechnology, Biol. Med.*, vol. 7, no. 4, pp. 385–402, 2011, doi: 10.1016/j.nano.2010.12.006.

[10] I. B. Bwatanglang *et al.*, "Folic acid targeted Mn:ZnS quantum dots for theranostic applications of cancer cell imaging and therapy," *Int. J. Nanomedicine*, vol. 11, pp. 413–428, 2016, doi: 10.2147/IJN.S90198.

[11] J. Singh and M. Rawat, “A Review on Zinc Sulphide Nanoparticles: From Synthesis, Properties to Applications,” no. December 2016, doi: 10.13188/2475-224X.1000006.

[12] B. P. Chandra, V. K. Chandra, and P. Jha, “Luminescence of II-VI semiconductor nanoparticles,” *Solid State Phenom.*, vol. 222, pp. 1–65, 2015, doi: 10.4028/www.scientific.net/SSP.222.1.

[13] G. J. Lee and J. J. Wu, “Recent developments in ZnS photocatalysts from synthesis to photocatalytic applications — A review,” *Powder Technol.*, vol. 318, pp. 8–22, 2017, doi: 10.1016/j.powtec.2017.05.022.

[14] S. Ghaderi, B. Ramesh, and A. M. Seifalian, “Fluorescence nanoparticles ‘quantum dots’ as drug delivery system and their toxicity: A review,” *J. Drug Target.*, vol. 19, no. 7, pp. 475–486, 2011, doi: 10.3109/1061186X.2010.526227.

[15] H. Hu and W. Zhang, “Synthesis and properties of transition metals and rare-earth metals doped ZnS nanoparticles,” *Opt. Mater. (Amst).*, vol. 28, no. 5, pp. 536–550, 2006, doi: 10.1016/j.optmat.2005.03.015.

[16] R. N. Bhargava, D. Gallagher, X. Hong, and A. Nurmikko, “Optical properties of manganese-doped nanocrystals of ZnS,” *Phys. Rev. Lett.*, vol. 72, no. 3, pp. 416–419, 1994, doi: 10.1103/PhysRevLett.72.416.

[17] A. A. Khosravi *et al.*, “Manganese doped zinc Sulphide nanoparticles by aqueous method,” *Appl. Phys. Lett.*, vol. 67, p. 2506, 1995, doi: 10.1063/1.114440.

[18] A. A. Khosravi *et al.*, “Green luminescence from copper doped zinc sulphide quantum particles,” *Appl. Phys. Lett.*, vol. 67, p. 2702, 1995, doi: 10.1063/1.114298.

[19] N. Karar, H. Chander, and S. M. Shivaprasad, “Enhancement of luminescent properties of ZnS:Mn nanophosphors by controlled ZnO capping,” *Appl. Phys. Lett.*, vol. 85, no. 21, pp. 5058–5060, 2004, doi: 10.1063/1.1815059.

[20] L. P. Wang and G. Y. Hong, “New preparation of zinc sulfide nanoparticles by solid-state method at low temperature,” *Mater. Res. Bull.*, vol. 35, no. 5, pp. 695–701, 2000, doi: 10.1016/S0025-5408(00)00261-0.

[21] P. Yang, M. Lu, D. Xu, D. Yuan, and G. Zhou, “ZnS nanocrystals co-activated by transition metals and rare-earth metals - A new class of

luminescent materials," *J. Lumin.*, vol. 93, no. 2, pp. 101–105, 2001, doi: 10.1016/S0022-2313(01)00186-7.

[22] V. Stanić, T. H. Etsell, A. C. Pierre, and R. J. Mikula, "Sol-gel processing of ZnS," *Mater. Lett.*, vol. 31, no. 1–2, pp. 35–38, 1997, doi: 10.1016/S0167-577X(96)00237-6.

[23] D. Haranath, N. Bhalla, H. Chander, Rashmi, M. Kar, and R. Kishore, "Controlled growth of ZnS:Mn nanophosphor in porous silica matrix," *J. Appl. Phys.*, vol. 96, no. 11, pp. 6700–6705, 2004, doi: 10.1063/1.1806552.

[24] S. J. Xu, S. J. Chua, B. Liu, L. M. Gan, C. H. Chew, and G. Q. Xu, "Luminescence characteristics of impurities-activated ZnS nanocrystals prepared in microemulsion with hydrothermal treatment," *Appl. Phys. Lett.*, vol. 73, no. 4, pp. 478–480, 1998, doi: 10.1063/1.121906.

[25] J. Xuand W. Ji, "Characterization of ZnS nanoparticles prepared by new route," *J. Mater. Sci. Lett.*, vol. 18, no. 2, pp. 115–117, 1999, doi: 10.1023/A:1006606316840.

[26] F. A. La Porta *et al.*, "Synthesis of wurtzite ZnS nanoparticles using the microwave assisted solvo thermal method," *J. Alloys Compd.*, vol. 556, pp. 153–159, 2013, doi: 10.1016/j.jallcom.2012.12.081.

[27] C. N. Xu, T. Watanabe, M. Akiyama, and X. G. Zheng, "Artificial skin to sense mechanical stress by visible light emission," *Appl. Phys. Lett.*, vol. 74, no. 9, pp. 1236–1238, 1999, doi: 10.1063/1.123510.

[28] K. Bogutska, Y. Sklyarov, and Y. Prylutskyy, "Zinc and zinc nanoparticles: biological role and application in biomedicine," *Ukr. bioorganicaacta*, vol. 1, pp. 9–16, 2013.

[29] J. Yang*et al.*, "Mesoporous zinc-blende ZnS nanoparticles: Synthesis, characterization and superior photocatalytic properties," *Nanotechnology*, vol. 19, no. 25, 2008, doi: 10.1088/0957-4484/19/25/255603.

[30] M. J. Ruedas-Rama, J. D. Walters, A. Orte, and E. A. H. Hall, "Fluorescent nanoparticles for intracellular sensing: A review," *Anal. Chim. Acta*, vol. 751, pp. 1–23, 2012, doi: 10.1016/j.aca.2012.09.025.

[31] A. Sirelkhatim*et al.*, "Review on zinc oxide nanoparticles: Antibacterial activity and toxicity mechanism," *Nano-Micro Lett.*, vol. 7, no. 3, pp. 219–242, 2015, doi: 10.1007/s40820-015-0040-x.

[32] S. Gulati, M. Sachdeva, and K. K. Bhasin, “Capping agents in nanoparticle synthesis: Surfactant and solvent system,” *AIP Conf. Proc.*, vol. 1953, no. May 2018, doi: 10.1063/1.5032549.

[33] U. Sanyal, R. Datta, and B. R. Jagirdar, “Colloidal calcium nanoparticles: Digestive ripening in the presence of a capping agent and coalescence of particles under an electron beam,” *RSC Adv.*, vol. 2, no. 1, pp. 259–263, 2012, doi: 10.1039/c1ra00468a.

[34] C. C. Li, S. J. Chang, F. J. Su, S. W. Lin, and Y. C. Chou, “Effects of capping agents on the dispersion of silver nanoparticles,” *Colloids Surfaces A Physicochem. Eng. Asp.*, vol. 419, pp. 209–215, 2013, doi: 10.1016/j.colsurfa.2012.11.077.

[35] Q. Wei, S. Z. Kang, and J. Mu, “‘Green’ synthesis of starch capped CdS nanoparticles,” *Colloids Surfaces A Physicochem. Eng. Asp.*, vol. 247, no. 1–3, pp. 125–127, 2004, doi: 10.1016/j.colsurfa.2004.08.033.

[36] E. E. L. Tanner, K. Tschulik, R. Tahany, K. Jurkschat, C. Batchelor-McAuley, and R. G. Compton, “Nanoparticle Capping Agent Dynamics and Electron Transfer: Polymer-Gated Oxidation of Silver Nanoparticles,” *J. Phys. Chem. C*, vol. 119, no. 32, pp. 18808–18815, 2015, doi: 10.1021/acs.jpcc.5b05789.

[37] S. R. Barman, A. Nain, S. Jain, N. Punjabi, S. Mukherji, and J. Satija, “Dendrimer as a multifunctional capping agent for metal nanoparticles for use in bioimaging, drug delivery and sensor applications,” *J. Mater. Chem. B*, vol. 6, no. 16, pp. 2368–2384, 2018, doi: 10.1039/c7tb03344c.

[38] M. Aliofkhazraei, *Handbook of nanoparticles*. 2015.

[39] D. Sharma, S. Kanchi, and K. Bisetty, “Biogenic synthesis of nanoparticles: A review,” *Arab. J. Chem.*, vol. 12, no. 8, pp. 3576–3600, 2019, doi: 10.1016/j.arabjc.2015.11.002.

[40] S. Campisi, M. Schiavoni, C. E. Chan-Thaw, and A. Villa, “Untangling the role of the capping agent in nano catalysis: Recent advances and perspectives,” *Catalysts*, vol. 6, no. 12, pp. 1–21, 2016, doi: 10.3390/catal6120185.

[41] J. S. Kim *et al.*, “Toxicity and tissue distribution of magnetic nanoparticles in mice,” *Toxicol. Sci.*, vol. 89, no. 1, pp. 338–347, 2006, doi: 10.1093/toxsci/kfj027.

[42] T. J. Webster, D. Gorth, and D. Rand, “Silver nanoparticle toxicity in Drosophila: size does matter,” *Int. J. Nanomedicine*, p. 343, 2011, doi: 10.2147/ijn.s16881.

[43] C. Carlson*et al.*, “Unique cellular interaction of silver nanoparticles: Size-dependent generation of reactive oxygen species,” *J. Phys. Chem. B*, vol. 112, no. 43, pp. 13608–13619, 2008, doi: 10.1021/jp712087m.

[44] E. S. Kawasaki and A. Player, “Nanotechnology, nanomedicine, and the development of new, effective therapies for cancer,” *Nanomedicine Nanotechnology, Biol. Med.*, vol. 1, no. 2, pp. 101–109, 2005, doi: 10.1016/j.nano.2005.03.002.

[45] J. S. Carewand P. Huang, “Mitochondrial defects in cancer,” *Mol. Cancer*, vol. 1, pp. 1–12, 2002, doi: 10.1186/1476-4598-1-9.

[46] D. Pathania, M. Millard, and N. Neamati, “Opportunities in discovery and delivery of anticancer drugs targeting mitochondria and cancer cell metabolism,” *Adv. Drug Deliv. Rev.*, vol. 61, no. 14, pp. 1250–1275, 2009, doi: 10.1016/j.addr.2009.05.010.

[47] V. C. Fogg, N. J. Lanning, and J. P. Mackeigan, “Key Aspects of Mitochondrial Biology Altered glucose metabolism in cancer cells: the Warburg effect Cancers Sweet Tooth: Alterations in Glucose Metabolism Overview of normal glucose metabolism,” *Chin. J. Cancer*, pp. 1–14.

[48] U. E. Martinez-Outschoorn, M. Peiris-Pagés, R. G. Pestell, F. Sotgia, and M. P. Lisanti, “Cancer metabolism: A therapeutic perspective,” *Nat. Rev. Clin. Oncol.*, vol. 14, no. 1, pp. 11–31, 2017, doi: 10.1038/nrclinonc.2016.60.

[49] G. Solaini, G. Sgarbi, and A. Baracca, “Oxidative phosphorylation in cancer cells,” *Biochim. Biophys. Acta -Bioenerg.*, vol. 1807, no. 6, pp. 534–542, 2011, doi: 10.1016/j.bbabio.2010.09.003.

[50] R. Moreno-Sánchez, A. Marín-Hernández, E. Saavedra, J. P. Pardo, S. J. Ralph, and S. Rodríguez-Enríquez, “Who controls the ATP supply in cancer cells? Biochemistry lessons to understand cancer energy metabolism,” *Int. J. Biochem. Cell Biol.*, vol. 50, no. 1, pp. 10–23, 2014, doi: 10.1016/j.biocel.2014.01.025.

[51] M. Brandon, P. Baldi, and D. C. Wallace, “Mitochondrial mutations in cancer,” *Oncogene*, vol. 25, no. 34, pp. 4647–4662, 2006, doi: 10.1038/sj.onc.1209607.

[52] A. Chatterjee, E. Mambo, and D. Sidransky, “Mitochondrial DNA mutations in human cancer,” *Oncogene*, vol. 25, no. 34, pp. 4663–4674, 2006, doi: 10.1038/sj.onc.1209604.

[53] I. Brigger, C. Dubernet, and P. Couvreur, “Nanoparticles in cancer therapy and diagnosis,” *Adv. Drug Deliv. Rev.*, vol. 64, no. SUPPL., pp. 24–36, 2012, doi: 10.1016/j.addr.2012.09.006.

[54] J. Zielonka*et al.*, “Mitochondria-Targeted Triphenylphosphonium-Based Compounds: Syntheses, Mechanisms of Action, and Therapeutic and Diagnostic Applications,” *Chem. Rev.*, vol. 117, no. 15, pp. 10043–10120, 2017, doi: 10.1021/acs.chemrev.7b00042.

[55] G. Kroemer, L. Galluzzi, and C. Brenner, “Mitochondrial membrane permeabilization in cell death,” *Physiol. Rev.*, vol. 87, no. 1, pp. 99–163, 2007, doi: 10.1152/physrev.00013.2006.

[56] G. Battogtokh *et al.*, “Mitochondria-targeting drug conjugates for cytotoxic, anti-oxidizing and sensing purposes: current strategies and future perspectives,” *Acta Pharm. Sin. B*, vol. 8, no. 6, pp. 862–880, 2018, doi: 10.1016/j.apsb.2018.05.006.

[57] M. P. Murphy, “Targeting lipophilic cations to mitochondria,” *Biochim. Biophys. Acta -Bioenerg.*, vol. 1777, no. 7–8, pp. 1028–1031, 2008, doi: 10.1016/j.bbabio.2008.03.029.

[58] K. Hashimoto, P. Angiolillo, and H. Rottenberg, “Membrane potential and surface potential in mitochondria. Binding of a cationic spin probe,” *BBA - Bioenerg.*, vol. 764, no. 1, pp. 55–62, 1984, doi: 10.1016/0005-2728(84)90140-3.

[59] A. Ono, S. Miyauchi, N. Kamo, M. Demura, and T. Asakura, “Activation Energy for Permeation of Phosphonium Cations through Phospholipid Bilayer Membrane,” *Biochemistry*, vol. 33, no. 14, pp. 4312–4318, 1994, doi: 10.1021/bi00180a027.

[60] A. B. Chinen, C. M. Guan, J. R. Ferrer, S. N. Barnaby, T. J. Merkel, and C. A. Mirkin, “Nanoparticle Probes for the Detection of Cancer Biomarkers, Cells, and Tissues by Fluorescence,” *Chem. Rev.*, vol. 115, no. 19, pp. 10530–10574, 2015, doi: 10.1021/acs.chemrev.5b00321.

[61] M. Ferrari, “Cancer nanotechnology: Opportunities and challenges,” *Nat. Rev. Cancer*, vol. 5, no. 3, pp. 161–171, 2005, doi: 10.1038/nrc1566.

[62] P. Gao, W. Pan, N. Li, and B. Tang, “Fluorescentprobesfororganelle-targetedbioactivespeciesimaging,” *Chem. Sci.*, vol. 10, no. 24, pp. 6035–6071, 2019, doi: 10.1039/c9sc01652j.

[63] X. He, K. Wang, and Z. Cheng, “In vivo near-infrared fluorescence imaging of cancer with nanoparticle-based probes,” *Wiley Interdiscip. Rev. Nanomedicine Nanobiotechnology*, vol. 2, no. 4, pp. 349–366, 2010, doi: 10.1002/wnan.85.

[64] H. Labiadh, K. Lahbib, S. Hidouri, S. Touil, and T. BEN Chaabane, “Insight of ZnS nanoparticles contribution in different biological uses,” *AsianPac. J. Trop. Med.*, vol. 9, no. 8, pp. 757–762, 2016, doi: 10.1016/j.apjtm.2016.06.008.

[65] A. Amiri Zarandi, “Self-organization of an optomagnetic $CoFe_2O_4$-ZnS nanocomposite: Preparation and characterization,” *J. Mater. Chem. C*, vol. 3, no. 16, pp. 3935–3945, 2015, doi: 10.1039/c5tc00023h.

[66] M. Tavakkoli Yaraki, M. Tayebi, M. Ahmadieh, M. Tahriri, D. Vashaee, and L. Tayebi, “Synthesis and optical properties of cysteamine-capped ZnS quantum dots for aflatoxin quantification,” *J. Alloys Compd.*, vol. 690, no. September 2017, pp. 749–758, 2017, doi: 10.1016/j.jallcom.2016.08.158.

[67] L. N. Liu*et al.*, “A novel Zn(II) dithiocarbamate/ZnS nanocomposite for highly efficient Cr6+ removal from aqueous solutions,” *RSC Adv.*, vol. 7, no. 56, pp. 35075–35085, 2017, doi: 10.1039/c7ra04259

[68] I. B. Bwatanglang *et al.*, “Folic acid targeted Mn:ZnS quantum dots for theranostic applications of cancer cell imaging and therapy,” *Int. J. Nanomedicine*, vol. 11, pp. 413–428, 2016, doi: 10.2147/IJN.S90198.

[69] N. J. Pace and E. Weerapana, “Zinc-binding cysteines: diverse functions and structural motifs,” *Biomolecules*, vol. 4, no. 2, pp. 419–434, 2014, doi: 10.3390/biom4020419.

[70] Chemical Book, Mercaptoacetic acid (68-11-1) https://www.chemicalbook.com/SpectrumEN_68-11-1_IR1.htm

[71] R. Song, Y. Liu, and L. He, “Synthesis and characterization of mercaptoacetic acid-modified ZnO nanoparticles,” *Solid State Sci.*, vol. 10, no. 11, pp. 1563–1567, 2008, doi: 10.1016/j.solidstatesciences.2008.02.006.